

Source mechanisms of explosions at Stromboli Volcano, Italy, determined from moment-tensor inversions of very-long-period data

Bernard Chouet,¹ Phillip Dawson,¹ Takao Ohminato,² Marcello Martini,³ Gilberto Saccorotti,³ Flora Giudicepietro,³ Gaetano De Luca,⁴ Giuliano Milana,⁴ and Roberto Scarpa⁵

Received 8 April 2002; revised 16 August 2002; accepted 8 October 2002; published 15 January 2003.

[1] Seismic data recorded in the 2–30 s band at Stromboli Volcano, Italy, are analyzed to quantify the source mechanisms of Strombolian explosions during September 1997. To determine the source-centroid location and source mechanism, we minimize the residual error between data and synthetics calculated by the finite difference method for a point source embedded in a homogeneous elastic medium that takes topography into account. Two source centroids are identified, each representative of the distinct event types associated with explosive eruptions from two different vents. The observed waveforms are well reproduced by our inversion, and the two source centroids that best fit the data are offset 220 and 260 m beneath and ~ 160 m northwest of the active vents. The source mechanisms include both moment-tensor and single-force components. The principal axes of the moment tensor have amplitude ratios 1:1:2, which can be interpreted as representative of a crack, if one assumes the rock matrix at the source to have a Poisson ratio $\nu = 1/3$, a value appropriate for hot rock. Both imaged cracks dip $\sim 60^\circ$ to the northwest and strike northeast–southwest along a direction parallel to the elongation of the volcanic edifice and a prominent zone of structural weakness, as expressed by lineaments, dikes, and brittle structures. For our data set, the volume changes estimated from the moments are ~ 200 m³ for the largest explosion from each vent. Together with the volumetric source is a dominantly vertical force with a magnitude of 10^8 N, consistent with the inferred movement of the magma column perched above the source centroid in response to the piston-like rise of a slug of gas in the conduit. *INDEX TERMS:* 7215

Seismology: Earthquake parameters; 7280 Seismology: Volcano seismology (8419); 8414 Volcanology: Eruption mechanisms; *KEYWORDS:* very-long-period seismicity, moment tensor inversions, eruption mechanics

Citation: Chouet, B., P. Dawson, T. Ohminato, M. Martini, G. Saccorotti, F. Giudicepietro, G. De Luca, G. Milana, and R. Scarpa, Source mechanisms of explosions at Stromboli Volcano, Italy, determined from moment-tensor inversions of very-long-period data, *J. Geophys. Res.*, 108(B1), 2019, doi:10.1029/2002JB001919, 2003.

1. Introduction

[2] Unlike tectonic earthquakes, which usually can be adequately described by six moment-tensor components, a complete description of volcanic processes may additionally require consideration of three single-force components for complete description. For example, a volcanic eruption can induce a force system that consists of a contraction of the conduit/reservoir system in response to the ejection of fluid, and a reaction force from the eruption jet [Kanamori *et al.*, 1984]. Solutions including a combination of moment-tensor and single-force components were also obtained by *Ohmi-*

nato et al. [1998] in an analysis of very-long-period (VLP) signals associated with magma injection beneath Kilauea Volcano, Hawaii.

[3] Some volcanic processes can be described by a single-force mechanism only. An example is the traction-force model used by *Ukawa and Ohtake* [1987] to explain the source mechanism of a long-period (LP) event beneath Izu-Oshima Volcano, Japan. In this model, the single force is the drag force on the conduit walls associated with the flow of viscous liquid in a conduit, and elastic radiation from this drag force is directly related to the mass flux history. Other examples of single-force sources can be found in the 1980 eruption of Mount St. Helens [Kanamori and Given, 1982; Kawakatsu, 1989] and in the 1991 eruption of Pinatubo, Philippines [Kanamori and Mori, 1992; Widmer and Zürn, 1992]. Kanamori and Given [1982] analyzed ultra-long-period (ULP) (~ 200 s) Love and Rayleigh waves excited by the eruption of Mount St. Helens and determined that the source is a nearly horizontal force with a characteristic time constant of 150 s, which

¹U.S. Geological Survey, Menlo Park, California, USA.

²University of Tokyo, Tokyo, Japan.

³Osservatorio Vesuviano, Naples, Italy.

⁴Servizio Sismico Nazionale, Rome, Italy.

⁵Università di Salerno, Salerno, Italy.

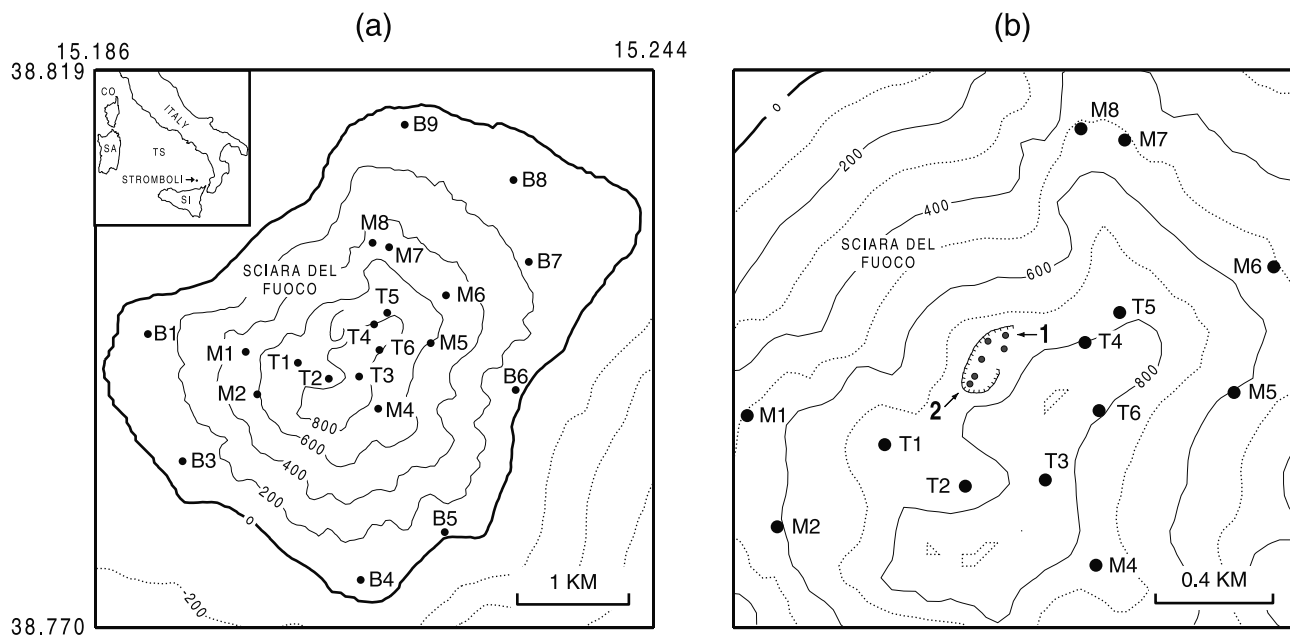


Figure 1. (a) Map of Stromboli Volcano showing locations of three-component broadband stations (solid dots) on Stromboli Volcano. Stations prefixed by “T” denote those of the “T ring” of sensors, by “M” those of the “M ring”, and by “B” those of the “B ring”, located at the top, midlevel, and base of the volcano, respectively. These designations are used in the analysis of the data and referred to in the Figures and text discussion. Contour lines represent 200 m contour intervals. The inset shows the location of Stromboli in the Tyrrhenian Sea (TS) in relation to Italy, Sicily (SI), Sardegna (SA), and Corsica (CO). (b) Detailed map of summit area showing seismic stations (solid dots) in relation to crater (ticked line) and eruptive vents (grey dots). The arrows point to the locations of the two active vents at the time of the experiment in September 1997. Contour lines represent 100 m contour intervals.

they attributed to the massive landslide observed at the time of the eruption [Voight *et al.*, 1981]. Kawakatsu [1989] reanalyzed the same data using a centroid single-force inversion technique and derived landslide parameters consistent with those obtained by Kanamori and Given [1982]. Mantle Rayleigh waves with periods near 230 s observed during the Mount Pinatubo eruption of 15 June 1991 were linked by Kanamori and Mori [1992] to an oscillatory vertical single force applied at the surface of Mount Pinatubo, which was attributed by these authors to the acoustic coupling of atmospheric oscillations triggered by the sustained thermal energy flux from the volcano. A single-force source model was also proposed by Uhira *et al.* [1994] to explain the mechanism of dome collapses at Unzen Volcano, Japan.

[4] Volumetric changes are commonly associated with mass transport in volcanoes and thus constitute an important class of sources associated with volcano dynamics. Uhira and Takeo [1994] showed that vulcanian explosions at Sakurajima Volcano, Japan, are accompanied by the contraction of a magma chamber at a depth of a few kilometers. A volume change was inferred for the source mechanism of phreatic eruptions at Aso Volcano, Japan, based on near-field broadband seismic observations [Kaneshima *et al.*, 1996; Legrand *et al.*, 2000; Kawakatsu *et al.*, 2000]. Nishimura *et al.* [2000] interpreted VLP data from Iwate Volcano, Japan, in terms of a mutual deflation and inflation of two connected magma chambers. Kumagai *et al.* [2001] inferred a volumetric source to be at the origin of the VLP

signals observed during caldera formation at Miyake Island, Japan. Solutions of moment tensor inversions including volume changes have also been obtained for geothermal systems [Julian *et al.*, 1997].

[5] Volcanic processes thus provide a rich assortment of seismic-source mechanisms, the study of which provides invaluable quantitative information on internal and external transport dynamics. In this paper, we use the linear inversion method of Ohminato *et al.* [1998] to investigate the source mechanism of VLP waveforms observed during explosive activity at Stromboli in September 1997. Synthetic waveforms are constructed by a superposition of impulse responses obtained for six moment-tensor components and three single-force components applied at a point source embedded in the 3D edifice of Stromboli. We begin with a brief description of the setting of Stromboli and of the broadband network and data recorded in September 1997, and proceed with an application of the inversion method to these data. We conclude with a discussion of the implications of these models for transport dynamics associated with Strombolian explosions.

2. Stromboli Volcano

[6] Located at the northern end of the Aeolian island arc in the Tyrrhenian sea off the southern coast of Italy, the volcanic island of Stromboli rises approximately 3000 m from the seafloor, with its summit 924 m above sea level (Figure 1a). The twin peaks forming the summit of the

volcano are remnants of the rim of an older crater. The current activity originates in vents located within a 250-m-long by 150-m-wide crater on a terrace northwest of, and about 130 m below, the northern peak (Figure 1b). The crater is buttressed by nearly vertical walls on the southeastern side and merges into a long talus slope on the northwestern side. This talus partially fills a large sector graben called the “Sciara del Fuoco” that extends from the summit to the sea.

[7] Stromboli is considered one of the most active volcanoes in the world, and its persistent but moderate explosive activity, termed “Strombolian”, is only interrupted by occasional episodes of more vigorous activity accompanied by lava flows, as last seen in 1975 [Capaldi *et al.*, 1978] and 1985. The present volcanic edifice is at least 100 kyr old and is the result of several growth stages involving seven distinct eruptive cycles [Hornig-Kjarsgaard *et al.*, 1993]. Individual growth stages all appear to be controlled by a NE–SW-trending zone of structural weakness, as evidenced by the predominant direction of lineaments, dikes, and brittle structures [Pasquaré *et al.*, 1993]. The morphology of the northwest flank of the volcano is dominated by the Sciara del Fuoco, whose formation is attributed to a giant sector collapse and landslide that occurred less than 5 kyr ago [Pasquaré *et al.*, 1993; Tibaldi, 2001]. Bathymetric studies by Romagnoli *et al.* [1993] indicate that the Sciara extends below sea level to a depth of about 1700 m. The present eruptive behavior, first described by Aristotle 2000 years ago, is characterized by mild, intermittent explosive activity, during which well-collimated jets of gases laden with molten lava fragments burst in short eruptions, each lasting 5–15 s and occurring at a typical rate of 3–10 events per hour [Chouet *et al.*, 1974]. Photoballistic analyses of single eruptions with durations of 10 s have yielded estimates of the mass of ejected fragments of 10^2 – 10^4 kg [Chouet *et al.*, 1974; Ripepe *et al.*, 1993], and volume of gas ejected on the order of 10^3 m³ [Chouet *et al.*, 1974].

[8] Persistent eruptive activity and ease of access make this volcano an ideal laboratory for detailed seismic measurements of the wave fields radiated by Strombolian activity. Much effort has been extended in recent years to gain a better understanding of the short-period (0.1–1 s) components of these wave fields [Del Pezzo *et al.*, 1992; Braun and Ripepe, 1993; Ripepe and Braun, 1994; Ripepe *et al.*, 1996; Chouet *et al.*, 1997; Saccorotti *et al.*, 1998; Ripepe and Gordeev, 1999; Saccorotti and Del Pezzo, 2000; Ripepe *et al.*, 2001]. These studies have shed light on some features of the seismic activity of Stromboli, which is mainly characterized by very shallow seismicity (<1 km depth) associated with eruptive activity, and by continuous volcanic tremor. Based on data from small-aperture arrays, Chouet *et al.* [1997] inferred that the sources of tremor and explosions are concentrated at depths shallower than 200 m beneath the summit crater. Similar analyses of array data by Saccorotti *et al.* [1998] and Saccorotti and Del Pezzo [2000] confirmed the very shallow origin of these sources. In contrast, relatively little is known of the longer-period (>1 s) characteristics of the eruption signals. Initial broadband observations carried out by Neuberg *et al.* [1994] indicated that Strombolian eruptions can produce signals with periods extending up to 10 s or more, and pointed to a shallow source region beneath the Sciara Del Fuoco con-

sistent with results based on short-period data. Wassermann [1997] used beam-forming analyses of waves in the frequency range of 0.3–0.9 Hz to locate a similar source region beneath the northwest flank of Stromboli. Based on tilt signals recorded at periods longer than 50 s on horizontal components of broadband seismometers, Wielandt and Forbriger [1999] inferred a source in the upper 100 m of the volcanic conduit. A more recent study of particle motions of very-long-period (VLP) waves from explosions [Kirchdörfer, 1999] has also documented a source region located between 50 and 200 m beneath the crater terrace.

2.1. Broadband Seismic Network

[9] Our data were recorded by a network of 21 three-component Guralp CMG-40T broadband (0.02–60 s) seismometers (see Figure 1a). The receiver layout was selected to provide homogeneous coverage in both azimuth and distance for sources located at shallow depths beneath the summit crater. The network featured three rings of sensors surrounding the edifice at crater level, midflank elevations, and near sea level, with stations ranging in distance between 0.3 and 2.2 km from the active crater. Data were recorded by 10 Lennartz Mars-Lite and 9 Kinometrics Altus-K2, 20-bit digital recorders operating at 125 and 100 samples s⁻¹ channel⁻¹, respectively, and also two Lennartz Mars-88, 16-bit digital recorders operating at 125 samples s⁻¹ channel⁻¹ at two of the lower stations. Both Mars-Lite and Altus K-2 data loggers used a Global Positioning System (GPS) time base with an accuracy of 5 μ s. Absolute time on the two Mars-88 recorders was achieved by synchronizing the internal clock with a DCF (Deutschland C-band Frankfurt) radio code.

[10] All the receivers were positioned with GPS with an accuracy of 5 cm in absolute location. The orientation of horizontal components was obtained by field measurements with compass and checked with GPS readings performed along a 20-m-long line extending through the north component of each receiver, yielding a precision of angular measurement within 2°. Amplitude and phase responses of the system components were first derived analytically and later confirmed by field calibrations. The seismic network operated from 18 September through 25 September 1997.

3. Strombolian Activity in September 1997

[11] Explosions at Stromboli typically occur at a rate of 3–10 events per hour [Chouet *et al.*, 1974], with occasional swarm activity reaching 20–30 events per hour. Strombolian activity in September 1997 during the seismic experiment was characterized by swarm activity. Figure 2a shows an hour-long sample of data representative of the activity observed at the time. The record is characterized by explosion signals superposed on a sustained background of tremor. The seismograms of Strombolian explosions are generally emergent and have typical durations of 10–20 s.

[12] Figure 2b shows the same record as in Figure 2a band-pass filtered between 2 and 30 s with a 2-pole zero-phase-shift Butterworth filter. This record enhances the very-long-period (VLP) components present in the explosion signals and displays the repetitive action of two sources distinguished by their characteristic waveforms. Eruptive activity during our experiment occurred mostly at two

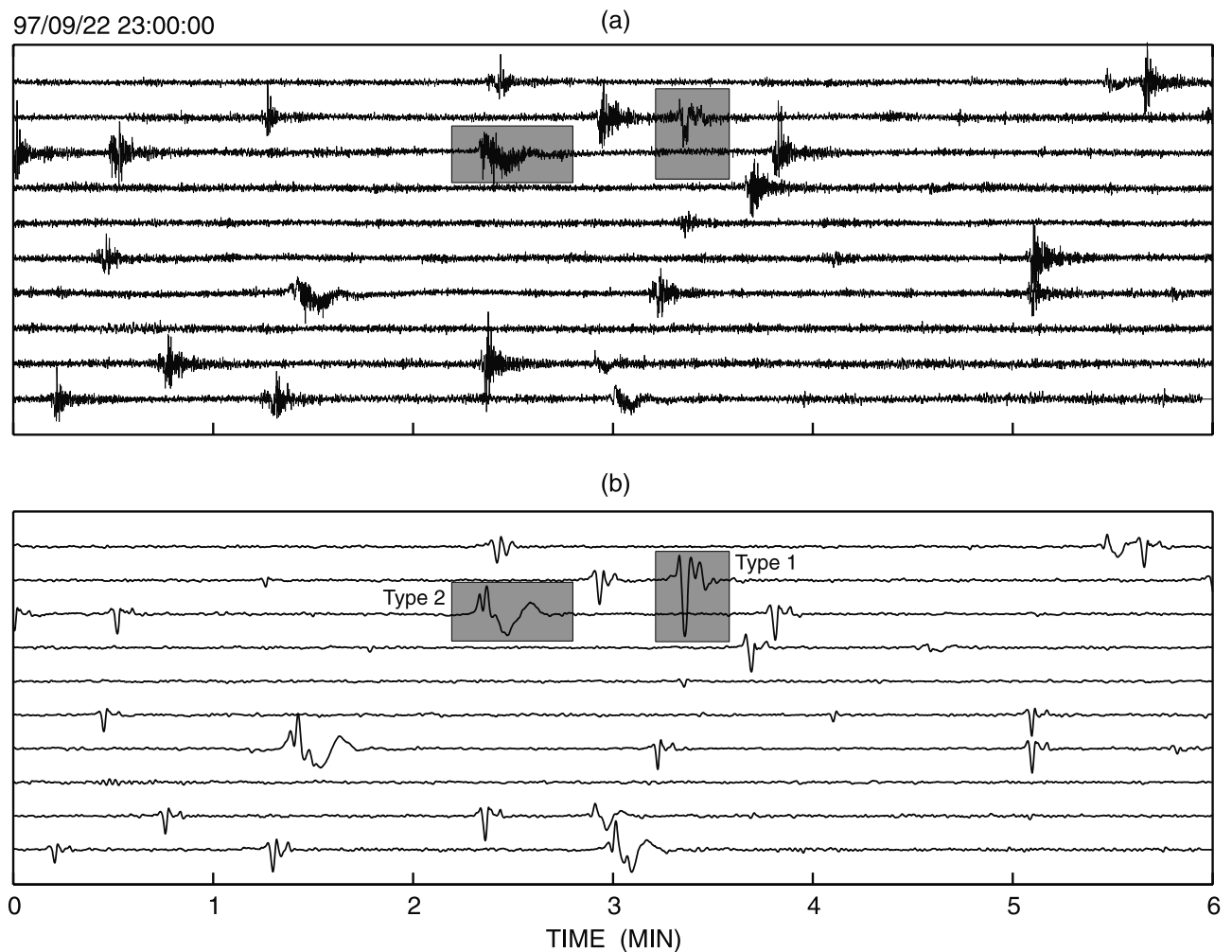


Figure 2. (a) Hour-long record of the east component of velocity at station T6 (see Figure 1 for location). The date and time (UT) at the start of the record are indicated at the upper left. (b) Record obtained by band-pass filtering the data in (a) in the 2–30 s band. Notice the repetitive action of two distinct sources identified in grey boxes as Type-1 and Type-2 events. The records in (a) and (b) are representative of true ground motion after deconvolution for instrument response.

distinct vents located near the northern and southern perimeters of the crater (vents 1 and 2 in Figure 1b), and the two types of waveforms illustrated in Figure 2b are representative of eruption signals from these vents. Type-1 events are associated with eruptions from the northern vent (vent 1). These eruptions were characterized by canon-like blasts typically lasting a few seconds and producing well-collimated jets of incandescent gases laden with molten fragments. Type-2 events are representative of eruptions from the southern vent (vent 2), which were much less impulsive than those from vent 1, lasted longer (up to 20 s), and produced wider fans of ejecta and significant amounts of ash.

[13] Oceanic microseismic noise was low during our experiment as demonstrated in the low background noise and good signal-to-noise ratios observed in the explosion waveforms, whose periods are overlapping the typical 3–7 s band of oceanic noise.

3.1. Character of Observed Broadband Waveforms

[14] Figure 3a illustrates a 7-min-long record for a sequence of four Type-1 and one Type-2 explosion events.

Spectrograms for both event types display energy concentrated in the VLP band. The Type-1 event contains strong spectral peaks in the 2.5–10 s (0.4–0.1 Hz) band. The Type-2 event also contains a weaker spectral peak near 2.5 s (0.4 Hz) and has another much stronger spectral peak near 14 s (0.07 Hz). Each eruption radiates elastic energy extending over the entire bandwidth displayed and probably beyond this bandwidth as well. Figure 3b shows details of the broadband signals and their VLP waveforms for both eruption types. The VLP signals are obtained by band-pass filtering the raw data with a 2-pole zero-phase-shift Butterworth filter and faithfully reproduce the VLP components present in the broadband data.

[15] The characteristics of all other explosion signals recorded are similar to either one or the other of the two events described above (Figure 4a). These similarities among VLP waveforms from different events clearly reflect a repetitive, nondestructive process at the source. The signal amplitude is the only parameter that changes from event to event in Type-1 explosions (see Figure 2b). Although there is more variability in the waveforms of Type-2 events, espe-

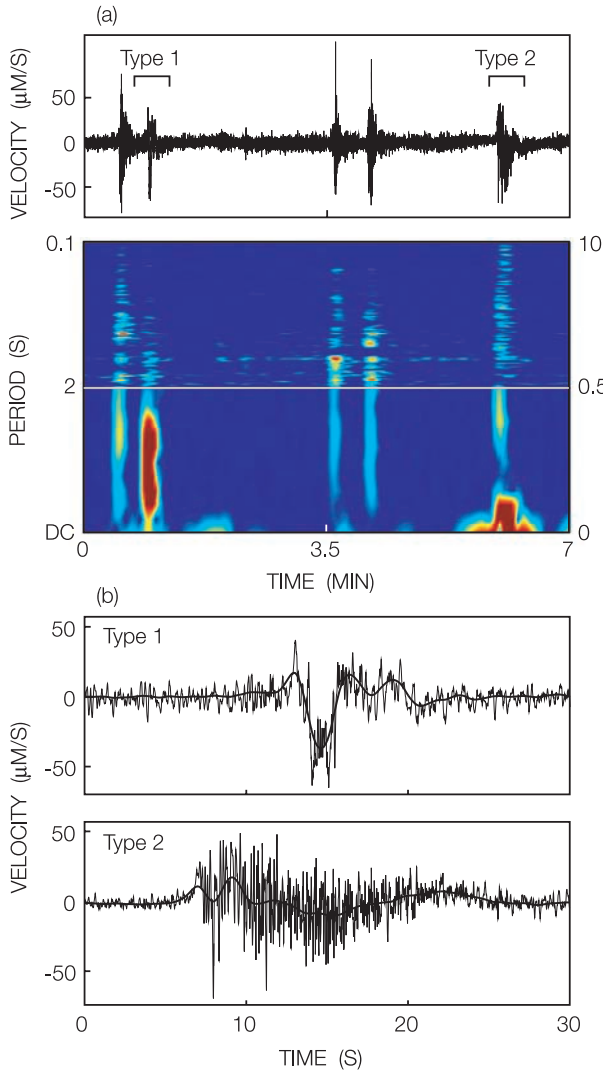


Figure 3. (a) East component of velocity at station T6 (top) and corresponding spectrogram (bottom) for two types of events (Type 1 and Type 2) obtained from a 20-s-long window sliding in increments of 2 s along this trace. The period axis is partitioned into two linear segments—ranging from DC (static) to 2 s (frequency from 0 to 0.5 Hz) and from 2 to 0.1 s (frequency from 0.5 to 10 Hz), respectively—to emphasize the very-long period content of the signal but still show the period contents of the signal down to 0.1 s. Each spectrum has been individually normalized. Warm colors (yellow, orange, and red) define the dominant spectral amplitudes; cooler colors (green, light to dark blue) define lower amplitudes and background. Each explosion radiates elastic energy over a wide band extending down to 0.1 s. (b) Detail of filtered (bold line) overlaid on broadband (thin line) east component of velocity recorded at station T6 for Type-1 and Type-2 explosion signals marked by brackets in the top panel of (a). The data in (a) and (b) are representative of true ground motion after deconvolution for instrument response.

cially during the later phases of these eruptions (Figure 4a), the signal onsets are also similar from event to event, again consistent with the repetitive action of a nondestructive source.

[16] The VLP waveforms recorded in our experiment are similar to those obtained from broadband measurements carried out at Stromboli in 1995 and 1996 by *Kirchdörfer* [1999], although the recovered bandwidth of our signals after deconvolution for instrument response is significantly less than that of the signals observed in the previous experiments. *Kirchdörfer* [1999] used sensors with period extending up to 120 s and observed four distinct types of events, all with a similar compression-dilatation-compression displacement sequence. These three characteristic phases are also present in the displacement signals we observe (Figure 4b), however with some notable differences. The main differences between our signals and those obtained by *Kirchdörfer* [1999] are in the durations of the initial compression phases, which typically last from 20 to 70 s in the 1995–1996 data compared to about 5 s for the Type-1, and 15 s for the Type-2 events observed in 1997. Diurnal temperature variations and other environmental inputs may have contributed to our limited ability to recover a clear signal at periods extending to the full 60 s of our sensor response. However, part of the differences in the recorded signals may also be due to differences in eruptive styles. The rate of explosions in September 1997 was

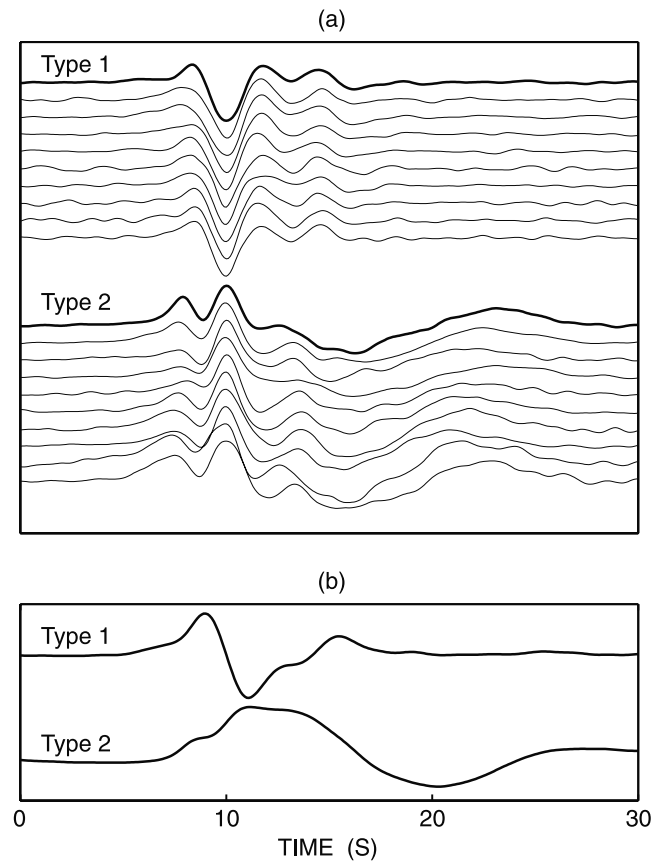


Figure 4. (a) Normalized east component of velocity seismograms recorded at station T6 for 10 Type-1 events and 10 Type-2 events selected from a 7-hour-long record. The traces are filtered between 2 and 20 s (Type 1) or 2 and 30 s (Type 2) to extract the VLP signals. (b) Normalized east component of displacement seismograms at station T6 for the two events marked by bold lines in (a). The waveforms have been corrected for instrument response.

elevated above normal, with roughly one event every 2–3 min on average compared to the typical activity of 3–10 events per hour. It is also possible that the 1997 eruptions were significantly smaller and more impulsive than those recorded in 1995 and 1996. A quantification of source parameters associated with such temporal evolution in eruptive style would naturally constitute an important objective toward gaining a better understanding of the long-term processes controlling Strombolian eruptions and improving our assessment of hazards posed by rare paroxysmal explosions. Such endeavor, however, is beyond the scope of the present study, which is limited to analyses of VLP waveforms from events representative of the two types of explosions observed during the course of our week-long experiment. Based on our observation that all the VLP waveforms in events of a given type have similar shapes, we infer that the operative source processes are essentially stationary with time within the bandwidth of our VLP data; thus an analysis of representative events is adequate to fully describe the overall source dynamics.

4. Source Location Estimated From Particle Motions

[17] The emergent aspect of the VLP waveforms (e.g., Figures 3–4) precludes the use of a conventional phase-pick method to locate the source of these signals. In our favor, however, is the observation that the waveforms are characterized by nearly linear particle motions at receivers in the T and M rings. Figure 5a shows particle motions obtained in the 2–20 s band for a Type-1 event, and Figure 5b illustrates a similar example obtained in the 2–30 s band for a Type-2 event. Horizontal and vertical particle motions all point to a small region northwest of the crater. These attributes were used by *Chouet et al.* [1999], who obtained an initial estimate of source location based on analyses of semblance [*Kawakatsu et al.*, 2000] and particle motions.

[18] Although not as linear, horizontal particle motions observed on receivers of the B ring generally point toward the same epicentral location beneath the Sciara del Fuoco. Interestingly, however, particle motions obtained on some of the B-ring receivers display a distinctive bent in the vertical-radial plane. For example, at receiver B4 (Figure 5a) the particle motion points to two directions, one of which is consistent with the position of the shallow source inferred from semblance analyses [e.g., *Chouet et al.*, 1999, Figure 5], while the other points to a deeper source region near sea level. Other receivers on the B ring also show evidence of a deeper source. The evidence for deeper components in the source dynamics during eruptions is not unexpected if one considers the associated process of mass removal. As gases escape from the top of the conduit, liquid magma within the conduit moves into the void left by the escaping gases. Although this process mostly disrupts the column of liquid perched above the location where the gas slug is released, it is also expected to induce weaker fluid motions in the deeper reaches of the conduit below the region of slug release. In view of their locations near sea level, it is therefore natural to expect that receivers on the bottom ring may be more sensitive to and detect these deeper components of the eruption process. Semblance analyses of the B-ring data suggest that the disruption of the fluid column

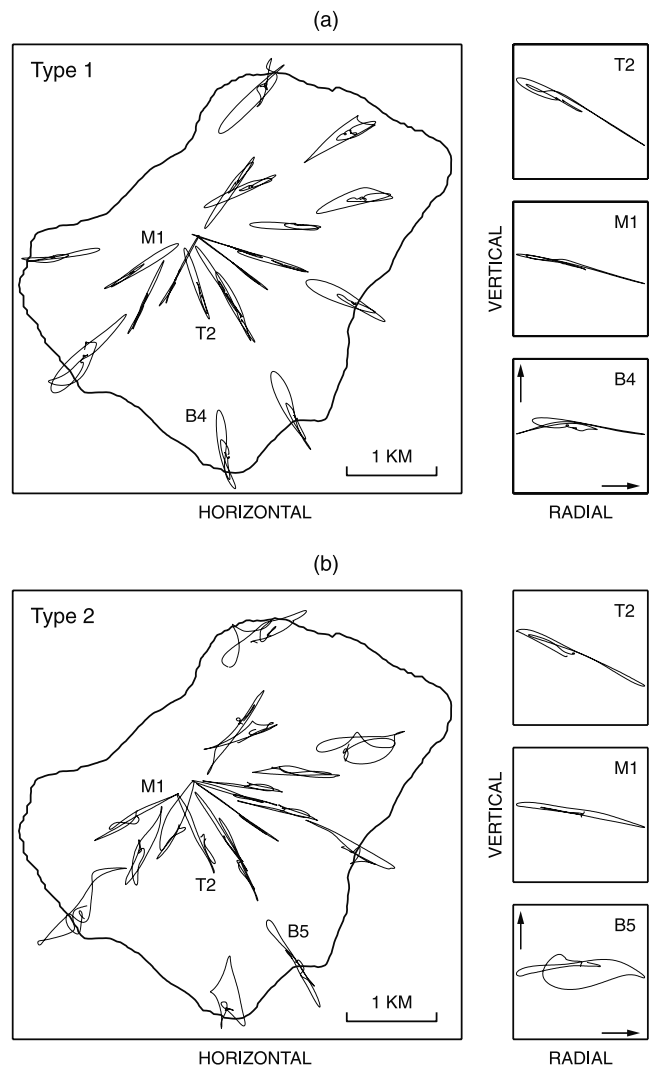


Figure 5. Normalized particle velocities observed on the network. (a) Particle trajectories in the horizontal (left panel) and vertical-radial (right) planes for a Type-1 event. The positive radial direction in the vertical-radial plane points to the source (see arrows in plot at lower right). (b) The same as (a) for a Type-2 event.

caused by eruptions may extend down to a few hundred meters below sea level.

[19] Compared to records from receivers on the T and M rings, the signal amplitudes measured on the B-ring receivers are 2–10 times smaller. Accordingly, the deeper source components evidenced in B-ring records may be viewed as being of second order compared to the shallow components of source process imaged by receivers of the top two rings. Below, we make full use of this observation and **focus our attention on records obtained at stations of the T and M rings** to quantify the source mechanism representative of the maximum moment release in the process driving the explosions at Stromboli.

5. Inversion Method

[20] The displacement field generated by a seismic source is described by the representation theorem which,

for a point source, may be written as [Chouet, 1996, equation (8)]

$$u_n(t) = F_p(t) * G_{np}(t) + M_{pq}(t) * G_{np,q}(t), \quad p, q = x, y, z, \quad (1)$$

where $u_n(t)$ is the n -component of seismic displacement at a receiver at time t , $F_p(t)$ is the time history of the force applied in the p -direction, $M_{pq}(t)$ is the time history of the pq -component of the moment tensor, and $G_{np}(t)$ is the Green tensor which relates the n -component of displacement at the receiver position with the p -component of impulsive force at the source position. The notation q indicates spatial differentiation with respect to the q -coordinate and the symbol $*$ denotes convolution. Summation over repeated indices is implied. This equation may be rewritten in the following simpler form [Ohminato et al., 1998]

$$u_n(t) = \sum_{i=1}^{N_m} m_i(t) * G_{ni}(t) = \sum_{i=1}^{N_m} \int_{-\infty}^{\infty} m_i(\tau) G_{ni}(t - \tau) d\tau, \quad (2)$$

where $m_i(t)$ is the time history of the i -th moment tensor or single force component at the source, $G_{ni}(t)$ are the Green's functions corresponding to each of the respective moment tensor and single force components, and N_m is the number of source mechanism components. The moment tensor and force components in equation (2) are defined as

$$\begin{aligned} m_1 &= M_{xx}, & m_2 &= M_{yy}, & m_3 &= M_{zz}, \\ m_4 &= M_{xy} = M_{yx}, \\ m_5 &= M_{yz} = M_{zy}, \\ m_6 &= M_{xz} = M_{zx}, \\ m_7 &= F_x, & m_8 &= F_y, & m_9 &= F_z, \end{aligned} \quad (3)$$

and the Green's functions are given by

$$\begin{aligned} G_{n1} &= G_{nx,x}, & G_{n2} &= G_{ny,y}, & G_{n3} &= G_{nz,z}, \\ G_{n4} &= G_{nx,y} = G_{ny,x}, \\ G_{n5} &= G_{ny,z} = G_{nz,y}, \\ G_{n6} &= G_{nx,z} = G_{nz,x}, \\ G_{n7} &= G_{nx}, & G_{n8} &= G_{ny}, & G_{n9} &= G_{nz}. \end{aligned} \quad (4)$$

To invert our data with equation (2) we use the method of Ohminato et al. [1998], which is a variant of the original method of Kikuchi and Kanamori [1982, 1986, 1991]. In the approach of Ohminato et al. [1998], the source location is fixed and the unknown source time functions $m_i(t)$ are represented by series of regularly spaced elementary functions (given by equation (8) in section 6.1), each with a different amplitude and sign. Denoting $u_n(p\Delta t)$ as the p -th sample of the n -th calculated synthetic seismogram at time $t = p\Delta t$, we obtain the discretized form of (2) as [Ohminato et al., 1998]

$$u_n(p\Delta t) = \sum_{i=1}^{N_m} \sum_{k=1}^{N_\tau} m_i(k\Delta\tau) G_{ni}(p\Delta t - k\Delta\tau) \Delta\tau, \quad n = 1, \dots, N_t, \quad p = 1, \dots, N_s. \quad (5)$$

In this expression, $G_{ni}(p\Delta t - k\Delta\tau)$ represents the Green's function for the n -th trace due to the i -th source mechanism at time $p\Delta t$ time shifted by $k\Delta\tau$, N_t is the number of elementary

functions used to represent the source time function, N_t is the number of observed seismic traces, and N_s is the number of samples in each trace. Equation (5) may be written in matrix form

$$\mathbf{d} = \mathbf{G}\mathbf{m}, \quad (6)$$

in which \mathbf{d} represents the data vector with dimensions $N_t N_s$, \mathbf{G} is the matrix of Green's functions with dimensions $N_t N_s$ by $N_m N_\tau$, and \mathbf{m} is a vector with dimensions $N_m N_\tau$ containing the unknown source time functions. Minimization of the square of the residual vector between data and synthetics in (6) yields the solution

$$\mathbf{m} = (\mathbf{G}'\mathbf{G})^{-1} \mathbf{G}'\mathbf{d}, \quad (7)$$

where \mathbf{G}' is the transpose of matrix \mathbf{G} . In our application, the source location is fixed, and the amplitudes of all the elementary source pulses are determined simultaneously from the set of linear equations (7). Although it is straightforward to include multiple point-source locations as additional unknowns in this approach, the size of the matrix of normal equations $\mathbf{G}'\mathbf{G}$ increases linearly with the number of source locations considered, leading rapidly to excessive memory requirements. In our inversion of data from Stromboli, we conduct a grid search with respect to source location and determine the best solution for a single point source instead of performing a simultaneous inversion for multiple point sources.

6. Data Analysis

6.1. Assumptions

[21] Our inversions rely on a series of assumptions concerning the bandwidth of the signal, medium structure, source location, source extent, and source mechanism. Although contamination of our signals by oceanic noise is minimal, the sensors in our network show marked sensitivity to diurnal temperature variations and other environmental inputs at periods longer than 50 s. Furthermore, the signal-to-noise ratios are weak and unreliable at periods longer than 30 s. To lessen data contamination due to increased sensitivity to noise at periods longer than 30 s, we highpass the waveforms of Type-2 events at 30 s. We highpass the signals from Type-1 events at 20 s to account for the slightly narrower useful band of these signals. As our interest lies mostly in the character of the VLP waveforms, we also lowpass the data at 2 s. After instrument corrections, our data are thus reliable over the bands 2–20 s for Type-1, and 2–30 s for Type-2 events.

[22] Our displacement signals are composed of an initial compression phase, followed by a dilatation, followed by another compression (Figure 4b). Although previous observations at Stromboli by Kirchdörfer [1999] indicate that the initial compression can last up to 70 s, the sensors in our network do not provide a reliable response extending up to such periods. Accordingly, our analysis focuses on shorter period components of the signal as illustrated in Figure 4. For Type-1 events, we consider a 20-s-long window bracketing the event, and for Type-2 events we select a 60-s-long record section encompassing the dominant signal in this event.

[23] Our calculations of Green's functions assume a **homogeneous medium** and include **the topography and bathymetry of Stromboli** (see section 6.3). We use the structural data elaborated by *Chouet et al.* [1998] and assume a compressional wave velocity $V_p = 3.5$ km/s, shear wave velocity $V_s = 2$ km/s, and density $\rho = 2650$ kg/m³. Wavelengths corresponding to the period range 2–30 s of the observed signals span 4–100 km so that small-scale velocity heterogeneities are assumed to have negligible effect on our results. **Green's functions are convolved with a smoothing function** to insure the stability of the inversion. We use the cosine smoothing function

$$S(t) = \begin{cases} \frac{1}{2} \left[1 - \cos\left(\frac{2\pi t}{t_p}\right) \right], & 0 \leq t \leq t_p, \\ 0, & t > t_p, \end{cases} \quad (8)$$

in which $t_p = 0.5$ s for the Green's functions applied to Type-1 events, and $t_p = 2.0$ s for the Green's functions applied to Type-2 events. **The smoothed cosine function convolved with the Green's functions represents our elementary source time function**, and the true source time function is obtained by a superposition of these elementary functions (note that other smoothing functions shaped as Gaussian, or smoothed step functions may also be used as elementary source time functions with identical results). **No anelastic attenuation is included in our calculations of Green's functions**, because all the receivers in the Stromboli network are located within a fraction of wavelength from the source, and anelastic attenuation effects are negligible over such short distances.

[24] Although the pattern of particle motions recorded on our network is suggestive of a source of finite extent, accounting for this extent by considering a group of vertically distributed point sources makes our problem too large. As the amplitudes recorded on the B ring are 2–10 times smaller than the amplitudes recorded on the T and M rings, the signal contributions from parts of the source other than the centroid identified with data from the T and M rings are quite small. Therefore, we conclude that most of the energy radiated by the source appears to originate within a small volume located at shallow depth beneath the Sciarra Del Fuoco, and the contributions from the deeper parts of the conduit may be viewed as second-order.

[25] Using only stations from the T and M rings, for which maximum rectilinearity of particle motions was observed, *Chouet et al.* [1999] obtained semblance locations of the sources of Type-1 and Type-2 events some 300 m below and 300 m northwest of the active vents. Source locations derived from separate analyses performed for different events of the two types all scatter within 100 m of each other [*Chouet et al.*, 1999]. The source dimension estimated from the scatter among locations of individual events is $L \leq 0.1$ km, the shortest source-receiver distance is $r_0 \simeq 0.3$ km, and the shortest wavelength of S waves is $\lambda_{\min} = 4$ km. Therefore, the relation $L^2 \ll r_0 \lambda_{\min}$ holds, meaning that, even if the extent of the source of maximum energy release is finite, we can approximate this source by a point source [*Aki and Richards*, 1980, pp. 804 and 805]. In this study, we make no attempt to resolve all the details of the extended source beneath Stromboli but focus instead on

the shallow region of the source that releases most of the seismic energy in the VLP band. We approximate this source by a single point source, whose initial location is determined by matching synthetic particle motions produced by an isotropic source to the particle motions observed on the receivers of the T and M rings. The source location and source mechanism that provide the best fit to data from the T and M rings are then obtained by conducting a **fine-grid search around the initial source location**. Synthetics for the best fit source are also calculated at receivers on the B ring; however, these synthetics are only used for qualitative comparison with the actual motion recorded at these locations. The best fit source location is determined under the assumption of a mechanism composed of six moment-tensor components and three single-force components. These results are compared to fits obtained for the same best fit source location for two other assumed source mechanisms: (1) six moment-tensor components only, and (2) three single-force components only.

6.2. Squared Errors

[26] We use the following definitions of squared error in the evaluation of our results [*Ohminato et al.*, 1998]

$$E_1 = \frac{\sum_{n=1}^{N_r} \sum_{p=1}^{N_s} (u_n^0(p\Delta t) - u_n^s(p\Delta t))^2}{\sum_{n=1}^{N_r} \sum_{p=1}^{N_s} (u_n^0(p\Delta t))^2} \times 100, \quad (9)$$

and

$$E_2 = \frac{1}{N_r} \sum_{n=1}^{N_r} \left[\frac{\sum_{p=1}^3 \sum_{p=1}^{N_s} (u_n^0(p\Delta t) - u_n^s(p\Delta t))^2}{\sum_{p=1}^3 \sum_{p=1}^{N_s} (u_n^0(p\Delta t))^2} \right] \times 100, \quad (10)$$

where $u_n^0(p\Delta t)$ is the p -th sample of the n -th data trace, $u_n^s(p\Delta t)$ is the p -th sample of the n -th synthetic trace, N_r is the number of data traces, N_s is the number of samples in each trace, and N_r is the number of three-component receivers. **In equation (9), large-amplitude traces dominate the squared error**, and the squared error remains small even when mismatches are present between data and synthetics for stations with weak-amplitude signals, as long as the stations with large-amplitude signals are well matched by the synthetics. In equation (10), the squared error is normalized station by station so that stations with weak-amplitude signals contribute equally to the squared error as stations with large-amplitude signals.

6.3. Model of Stromboli Volcano

[27] To determine the source location and associated mechanism of Strombolian explosions we need to compare our observed data to synthetic data calculated for a realistic model of Stromboli. Synthetics are obtained by the three-dimensional finite difference method of *Ohminato and Chouet* [1997], in which the topography and bathymetry of Stromboli are discretized in a staircase by stacking unit cells with fixed cell size.

[28] The computational domain is centered on the edifice and has lateral dimensions of 9.8×9.8 km, and vertical

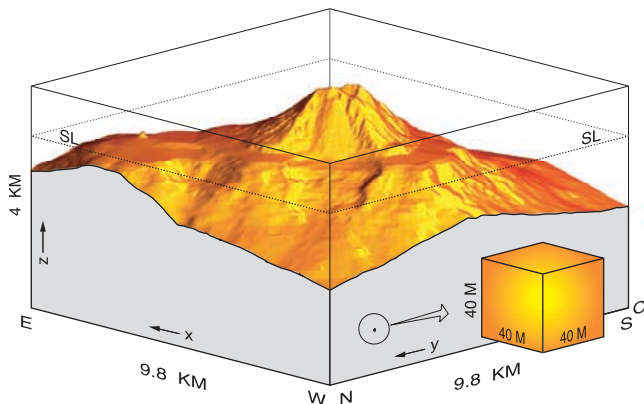


Figure 6. Extent of domain and grid size selected for finite difference calculations for Stromboli Volcano. Sea level (SL) is indicated by a dotted line. “O” marks the origin of the Cartesian coordinates used in the model.

extent of 4 km (Figure 6). Our calculations are performed over a grid of $40 \times 40 \times 40$ m, yielding a 3-D mesh with $246 \times 246 \times 101$ nodes. The grid size considered is small enough to satisfy the criterion of minimum number of grids per wavelength established by *Ohminato and Chouet* [1997], and the size of the computational domain is sufficiently large to minimize spurious edge reflections, yet small enough to preclude prohibitive calculations.

[29] The Cartesian coordinates are set with origin at the lower left corner of the domain, with x axis positive eastward, y axis positive northward, and z axis positive upward. The top boundary of the domain is set to coincide with the top of Stromboli. The summit of Stromboli is at an altitude of 924 m and for simplicity we use elevations above sea level rather than the actual z -coordinate above the base of the model when referring to the vertical position of a source in the edifice.

[30] The topography of Stromboli is obtained from a digital elevation map (DEM) of the island provided by G. Macedonio, Osservatorio Vesuviano, and the bathymetry of the submerged edifice is constructed from the data of *Gabbianelli et al.* [1993] and *Romagnoli et al.* [1993]. The resolution of the DEM is 25 m, and that of the bathymetry ranges from 25 m over the submerged extent of the Sciara Del Fuoco, to 100 m over the remainder of the submerged edifice. We resample these topographic and bathymetric data at 40 m to make them compatible with our computational mesh.

[31] The seawater surrounding the island of Stromboli is not included in our calculations of synthetic waveforms because this sea layer was found to have a negligible effect on our results. For example, using the centroid locations and source time functions obtained for our best models (see Figures 8, 11, and 12) as input source models, we compared synthetics calculated at receivers of the T, M, and B rings with and without this sea layer. No visible differences were observed in the waveforms calculated at stations of the T-ring with or without inclusion of this layer. The waveforms were left similarly unchanged on both the M and B rings, although small differences in signal amplitudes were noted at a few locations along these latter rings. The variations in peak amplitudes of the synthetics

amounted to less than 1% on the M-ring, and less than 2% on the B-ring.

6.4. Source Locations

[32] Our first objective is to delimit the extent of the source domain, within which the search for the best fit point source is to be conducted. This is achieved in two steps. First, we consider an isotropic point source with characteristic period similar to that of the observed signals and use trial-and-error to find the location of the point source that provides the best fit of synthetic particle motions to the data. This is done by calculating synthetics at each receiver in the T and M rings, and minimizing the error between the location of peak semblance calculated for the synthetics and peak semblance solution obtained by *Chouet et al.* [1999]. The synthetics are obtained for a source time function in the form of a Ricker wavelet

$$S(t) = \left\{ 2 \left[\frac{\pi(t-t_p)}{t_p} \right]^2 - 1 \right\} \exp \left\{ - \left[\frac{\pi(t-t_p)}{t_p} \right]^2 \right\} \quad (11)$$

with period $t_p = 3$ s similar to the dominant period observed in Type-1 events (see Figure 4a).

[33] Second, using the location of the best fit isotropic point source as our initial trial source location, we consider point sources distributed in a 3-D mesh surrounding this trial solution and search for the point source and associated mechanism that provide the best fit to the data. The source domain so investigated (illustrated in Figure 7) consists of a core of densely distributed nodes surrounded by a coarser distribution of nodes. In the core region, point sources are positioned at individual grid nodes spaced 40 m apart in a uniform mesh extending 160 m in the east–west and north–south directions, and from 240 to 600 m in elevation. In the surrounding region, point sources are spaced 80 m in a uniform mesh extending over 400 m in the east–west direction, 320 m in the north–south directions, and from 120 to 600 m in elevation. Because of the steep slope of the Sciara Del Fuoco, some of the nodes in the domain are located above the topography; these nodes are not used in our calculations of Green’s functions. The total number of point sources considered is 418.

[34] Green’s functions are calculated for all the network receivers for six moment-tensor components and three single-force components applied at each source node. Using data from the top two rings of receivers (T and M) only, we invert these data (see section 5) separately for each source node and evaluate the resulting source mechanism by computing squared errors according to the definitions in equations (9) and (10) (see section 6.2). The best fit point source location is the position at which the residual error between data and synthetics is minimum. The shape of the error region and source centroid corresponding to the minimum error are found by merging the results from the coarse and fine grids and interpolating to a uniform grid spacing of 20 m.

[35] Figure 8 illustrates the distributions of residual errors calculated with equation (10) for the two types of events, as represented by the largest explosions we observed in our data set (identified by the grey boxes in Figure 2). The error minimum for the Type-1 event yields a source centroid located at an elevation of 520 m, approximately 220 m

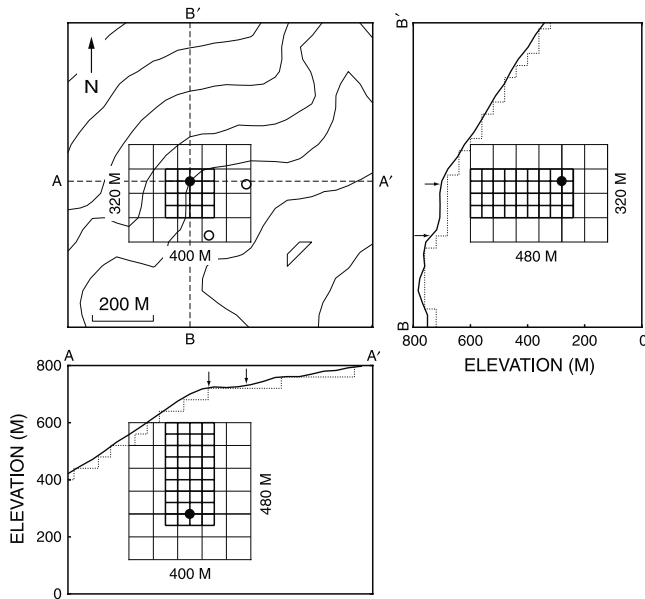


Figure 7. Horizontal, east–west and north–south vertical cross-sections through the source domain selected in our search of the best fit point source satisfying the data. The positions of the cross-sections are indicated by the dashed lines (AA' and BB') in the map view. The selected domain is bounded by the larger 400 × 320 × 480 m gridded region. Thin lines define a coarser 80 × 80 × 80 m grid, and bold lines define a finer 40 × 40 × 40 m grid. A solid dot marks the location of the initial isotropic point-source solution used to position the source domain of interest (see text for details). Contour lines in the map view represent 100-m contour intervals and open circles mark the positions of the two active vents. A dotted line shows the digitized topography profile in the vertical cross-sections, and arrows mark the projections of the two vents in these cross-sections.

below and 190 m west of vent 1. The error minimum for the Type-2 event points to a centroid at an elevation of 480 m, 40 m directly below the centroid of the Type-1 event and 190 m north–northwest of vent 2.

[36] Horizontal and vertical cross-sections through the two centroids provide measures of the relative positions of these centroids with respect to the active vents. Interestingly, the two centroids are positioned approximately 180 m south and up to 140 m shallower than the peak-semblance centroid locations determined by *Chouet et al.* [1999]. The marked difference between these solutions results from the strong distortion of the wave field caused by topography. The effect of topography was not accounted for in the original semblance solutions obtained by *Chouet et al.* [1999], but is fully included in the present calculations.

[37] As the two error definitions in equations (9) and (10) emphasize different aspects of the data, the best fit source locations derived by the two methods are slightly different (Table 1). For example, for the Type-1 event, the elevation of the best fit point source determined from the minimum in the squared error changes from 520 m for the more conservative error estimate E_2 based on equation (10) (Figure 8), to 560–600 m for estimate E_1 based on equation

(9). Error E_1 naturally yields a shallower source location estimate, because this error is most sensitive to the accuracy of the fits to waveforms recorded on the summit receivers, which are closest to the vents and are therefore most sensitive to near-field components of the wave field originating in the shallowest parts of the conduits. In that case,

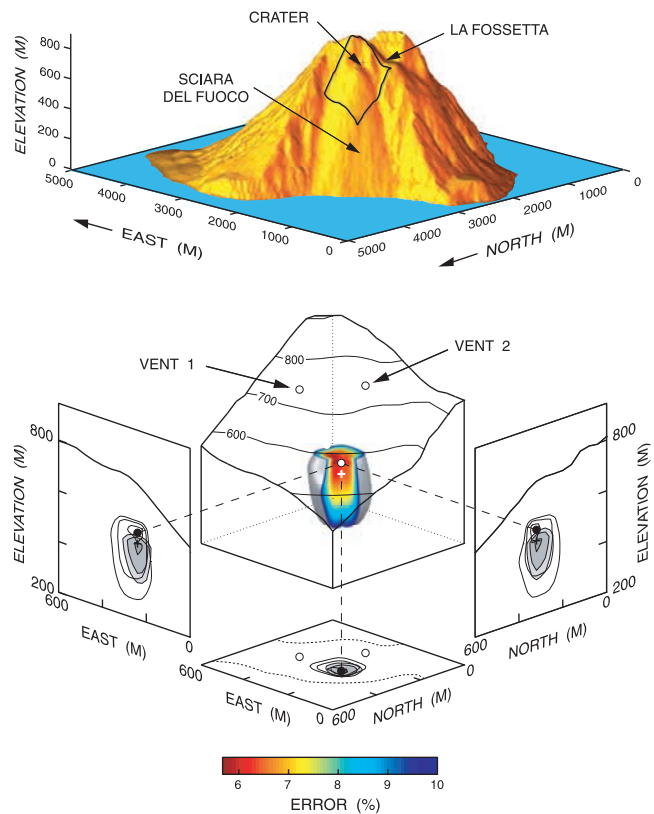


Figure 8. Source locations of the two types of events analyzed in this paper. A south-east looking view of Stromboli is shown at the top to help identify the location of the VLP sources within the volcanic edifice. The bold black line on the north-west flank of the edifice bounds the surficial extent of the domain considered in the bottom view. The cutaway view below shows the residual error region for Type-1 event, color-coded according to the magnitude of the error between data and synthetics (see text for details). The grey surface represents the outline of the error region, and the white dot shows the position of the source centroid corresponding to the minimum error; open circles indicate locations of the two vents on the surface. The side and bottom planes are east–west vertical, north–south vertical, and horizontal cross-sections through the source location. Contours on these planes are projections of the error region for the source location. Contours represent 6, 8, and 10% errors. A similar error region (not shown) was obtained for Type-2 event, whose centroid marked by a cross is located 40 m below the centroid of Type-1 event. The grey patches on the side and bottom planes represent 15, 16, and 17% error regions for the Type-2 event. Topographic contours (dotted lines) in the bottom plane are shown to better picture the source locations relative to the two active vents (open circles) projected vertically downward from the surface.

Table 1. Residual Errors E_1 and E_2 Calculated With Equations (9) and (10), Respectively, and Corresponding AIC Calculated With Equation (12) for the Three Source Mechanisms Considered in Our Inversions of Data for Stromboli Volcano

Source Mechanism	Error E_1 , %	Error E_2 , %	AIC(E_1)	AIC(E_2)
<i>Type-1 Event</i>				
Force Only	26.7	49.1	-48,501	-24,785
Moment Only	3.7	6.0	-122,591	-103,801
Moment and Force	3.1	5.2	-126,673	-106,538
<i>Type-2 Event</i>				
Force Only	32.7	67.7	-12,226	-3665
Moment Only	9.4	16.5	-25,977	-19,310
Moment and Force	6.7	14.2	-29,097	-20,223

waveforms on the T receivers are slightly better fitted while the fits obtained on the M ring are slightly worse. Error E_2 , however, appears to be most representative of a well-balanced quality of fits on all the receivers of the T and M rings. The source mechanisms calculated for each of the individual best fit locations are essentially indistinguishable.

[38] A similar behavior of error distribution is observed for the Type-2 event, for which the elevation of the absolute minimum in residual error changes from 480 m for estimate E_2 to 560–600 m for estimate E_1 .

6.5. Waveform Fits

[39] Figures 9 and 10 show the waveform matches obtained by inversion of the data for Type-1 and Type-2 events, respectively. Only data from the T and M rings are included in the fits, which are based on the assumption of a

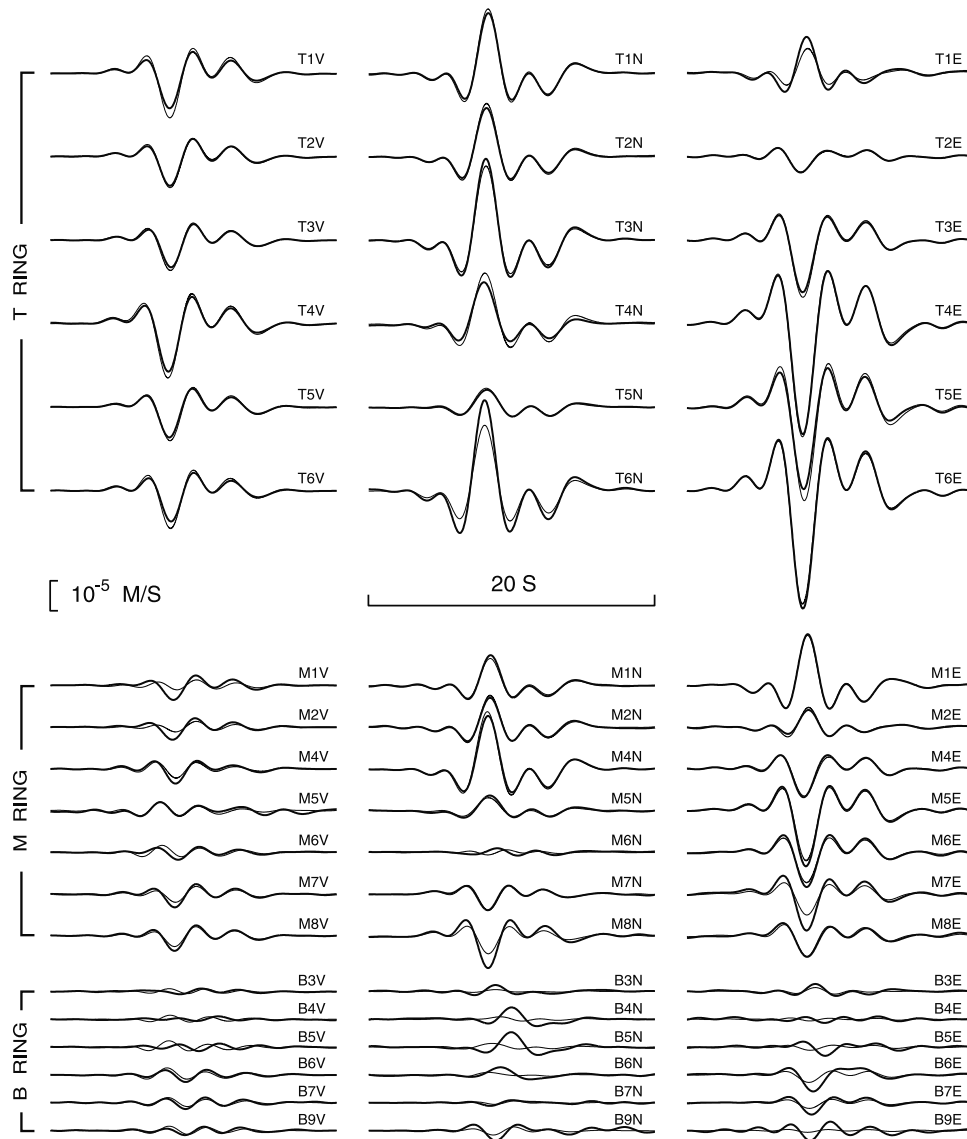


Figure 9. Waveform match obtained for a Type-1 event, in which six moment-tensor components and three single-force components are assumed for the source mechanism. Though shown (bottom of figure) the data from the B-ring receivers are not used in the inversion. Thin lines indicate synthetics, and bold lines represent observed velocity waveforms. The station code and component of motion are indicated at the upper right of each seismogram.

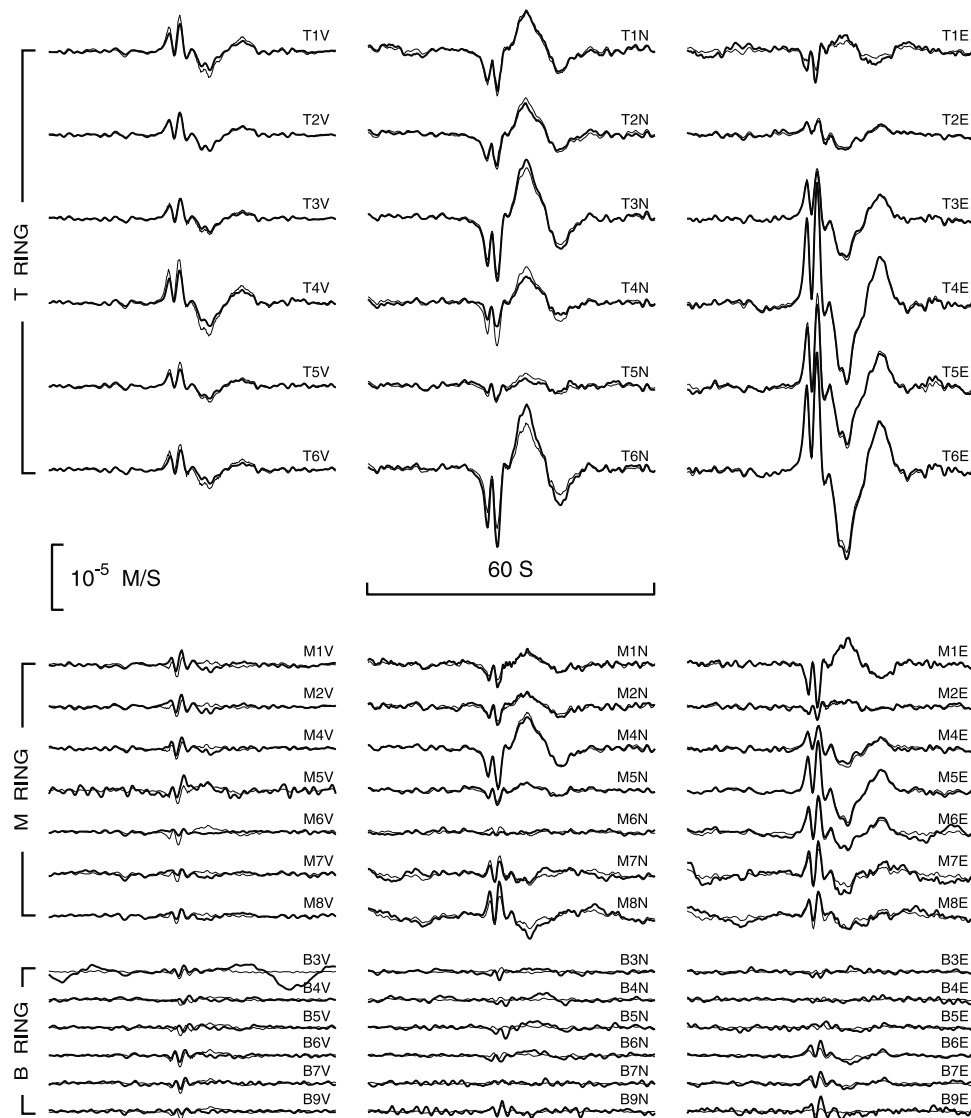


Figure 10. Same as Figure 9 for a Type-2 event.

source mechanism consisting of six moment-tensor components and three single-force components, and are representative of the best fit source centroids (Figure 8). The fits are excellent overall as demonstrated in the close match between waveforms and small values of residual errors listed in Table 1. Residual errors for the Type-2 event are larger than those associated with the Type-1 event, mainly because of the longer duration of record used in the fits and larger contribution of noise components in this window.

[40] As stated earlier, data from the B-ring receivers were not included in these inversions, because some of the stations on this ring show evidence for particle motions pointing to deeper source components as compared to data from the top two rings. Despite this limitation, our comparison of synthetics and data recorded at the B sites indicates that the waveform matches obtained on some components of these more distant stations are reasonable also. In particular, we note that the vertical components at stations B6, B7, and B9 are well matched for both types of events.

[41] To further test the effect of not including data from the B ring on our inversion results obtained with data from

the T and M rings only, we performed two inversions each including data from all three rings. For these test inversions, we again assumed a source mechanism consisting of six moment-tensor components and three single-force components and used the same best fit source location as in our earlier inversions. The waveform fits were found to be virtually unchanged with or without inclusion of the B-ring data; however, the residual errors were found to be consistently larger in fits including the B ring compared to fits excluding these data.

[42] Although not shown here, excellent fits were also obtained for the Type-1 event for a source mechanism represented by six moment-tensor components only (Table 1). Again, the fits obtained with or without data from the B ring were found to be virtually identical, indicative of the small relative importance of the B-site data in the solution. In contrast, fits obtained for Type-2 event for the same assumed source mechanism were observed to be markedly worse than the fits based on a combination of moment tensor and force components (Table 1). Fits based on a source consisting of three single-force components only were observed to be far

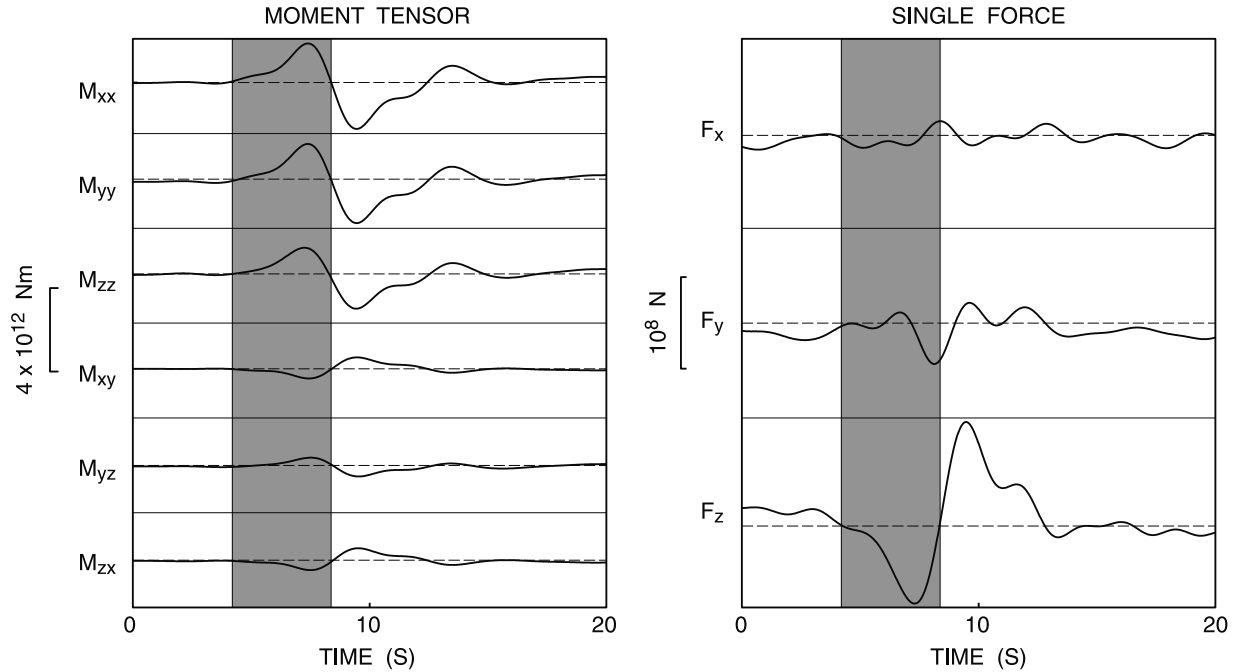


Figure 11. Source time functions obtained for the Type-1 event, in which six moment-tensor components and three single-force components are assumed for the source mechanism. Shading marks the interval during which the initial volumetric expansion of the source occurs (see text for explanations).

worse than fits obtained for moments only, or moments and forces, in both types of events as demonstrated by the larger residual errors in Table 1.

[43] In the Type-1 event, the residual errors estimated for a source mechanism limited to six moment-tensor components are within one percent of those estimated for a source mechanism including six moment-tensor components and three single-force components (Table 1). At first glance, the need for additional free parameters in the form of force components may appear to be open to question. However, the goodness of fit is not the only consideration in the selection of the best solution. Consistent waveform shapes among individual moment-tensor components are also required for a realistic interpretation of the source mechanism. Comparison of the moment tensor solutions, obtained with or without a single force, indicates that **the introduction of the force components is necessary to obtain a physically consistent source mechanism for Type-1 event.** In the Type-2 event, the errors are significantly reduced when both forces and moments are included in the model, so that the additional force parameters appear to be even more critical to the solution. To test the significance of the number of free parameters each source model was evaluated by calculating Akaike's Information Criterion (AIC) [Akaike, 1974] defined as

$$\text{AIC} = N_t N_s \ln E + 2N_m N_\tau, \quad (12)$$

in which the constant term is omitted. The parameter E in this equation represents the squared error defined according to equation (9) or (10). Table 1 lists the values of AIC estimated for the three models for both Type-1 and Type-2 events. The source model with six moment-tensor components and three single-force components consistently yields

the minimum values of the AIC for the two types of events analyzed (Table 1), supporting our contention that this is the most appropriate model to describe the source mechanism of these events. Thus, the force components do have significance from a physical viewpoint, and the error reduction is not merely a numerical artifact stemming from an increase in the number of free parameters in the model.

6.6. Source Mechanisms

[44] The source time functions associated with fits depicted in Figures 9 and 10 are shown in Figures 11 and 12, respectively; the volumetric components of the moment tensor clearly dominate in each solution. Eigenvectors determined for the solutions for Type-1 and Type-2 events are shown in Figure 13. The three eigenvectors identified by thick grey lines (Figures 13a and 13b) are obtained from measurements of the maximum peak-to-trough amplitudes in the individual tensor components (see Table 2); these are illustrated again in Figures 13c and 13d as bold arrows. The amplitude ratios of the principal axes of the moment tensor derived from these latter measurements are 1:0.8:2 and 1.1:1:2 in Type-1 and Type-2 events, respectively. The principal axes of the moment tensor for a tensile crack have amplitudes $\lambda\Delta V$, $\lambda\Delta V$, and $(\lambda + 2\mu)\Delta V$, in which ΔV represents the volume change associated with the crack opening/closure, and λ and μ are the Lamé coefficients of the rock matrix [Chouet, 1996, equation (15)]. **A Poisson ratio $\nu = 1/3$ for the rock implies $\lambda = 2\mu$,** so that the amplitude ratios of the principal axes of the moment tensor describing the crack become **1:1:2.** Therefore, our results may be viewed as approximating those for a crack, if one assumes a Poisson ratio $\nu = 1/3$ at the source - **a value appropriate for volcanic rock at or near liquidus temperatures [Murase and McBirney, 1973].**

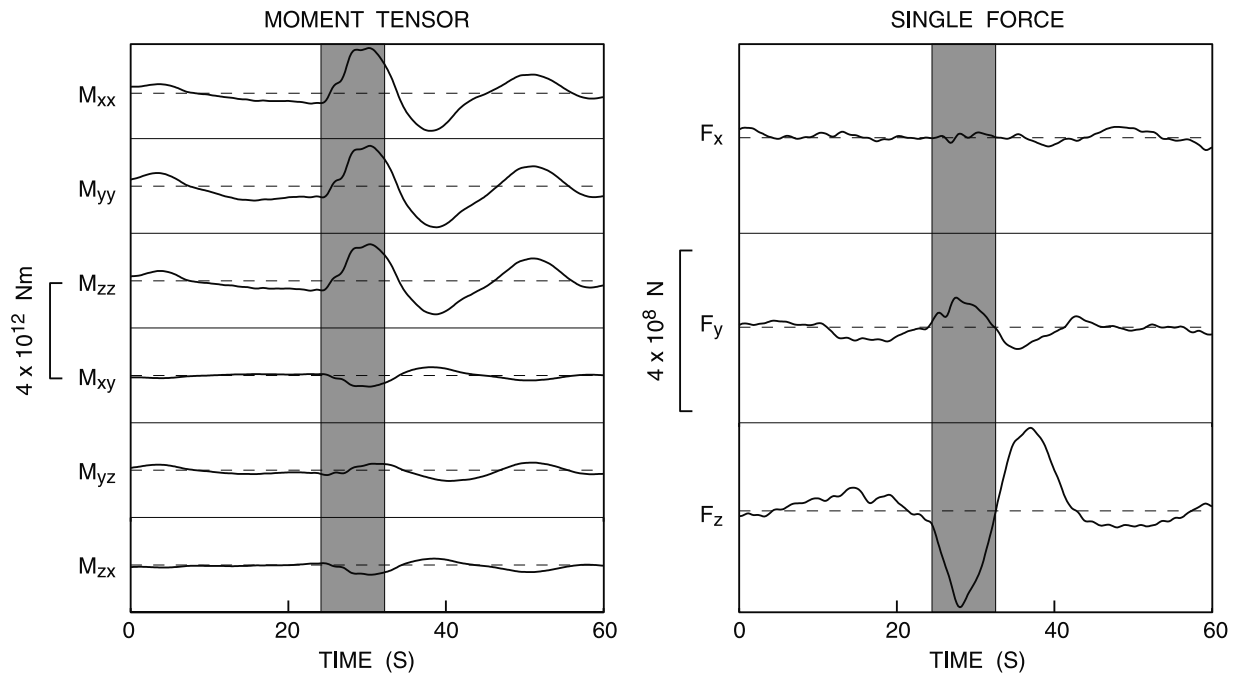


Figure 12. Same as Figure 11 for the Type-2 event. Notice the different time scale.

[45] Overall, the source mechanisms are robust. The directions of the eigenvectors and amplitude ratios of the principal axes of the moment tensor determined for the Type-1 event (Figure 13a) are both stable, indicating that the source mechanism is stationary with time. The amplitude ratios of the principal axes of the moment tensor are quite stable in the Type-2 event as well, although there is greater scatter in the directions of the eigenvectors for this event (Figure 13b) suggestive of source complexities not observed in Type-1 event. The slight rotation in the principal eigenvectors around the dominant directions imaged by the thick grey lines may be indicative of some curvature in the crack-like conduit, but this effect is not strong enough to be deemed significant. For both events, the directions of the eigenvectors and amplitude ratios of the principal axes of the moment tensor are well represented by the measurement of the maximum peak-to-trough amplitudes in the individual tensor components.

[46] The imaged crack for Type-1 event dips 63° to the northwest and strikes northeast-southwest along a direction parallel to the prominent NE-SW-trending zone of structural weakness and elongation of the volcanic edifice. The imaged crack for Type-2 event displays a slightly shallower northwest dip of 62° with a strike that differs by four degrees from that of the crack resolved for Type-1 event. In any case, both crack azimuths are fully consistent with the trends of exposed dikes and a known zone of weakness in the edifice [Pasquaré et al., 1993].

[47] No physically realistic solution is obtained when the source mechanism is limited to six moment-tensor components. In the Type-1 event, the source time functions of the M_{zz} , M_{yz} and M_{zx} components are different from the source time function shared by the M_{xx} , M_{yy} , and M_{xy} components, casting doubt on the results even though the amplitude ratios of the three principal axes of the moment tensor obtained from measurements of the maximum peak-to-trough amplitudes in the individual tensor components are essentially indistin-

guishable from those obtained with the solution including the single force. The source time functions in the Type-2 event obtained for a source limited to moments are similarly distorted so that no realistic mechanism can be inferred.

[48] The source time functions of the moment components for Type-1 event (Figure 11) show an initial inflation of the dike, followed by a deflation and terminating with a small reinflation pulse. The first inflationary phase is consistent with a pressurization of the dike associated with the formation and release of a slug of gas. The following deflationary phase reflects a depressurization of the dike in response to a decrease in magmastic head associated with the rise and ejection of the slug from the conduit, and the third and final phase points to a repressurization of the dike attributed to an increase in magmastic head due to slumping of the liquid film surrounding the slug back to the top of the magma column after the slug has burst at the surface.

[49] To estimate the volume change at the source, we need an appropriate value of μ in the source region. The value $\nu = 1/3$ suggests a value of μ smaller than $\mu = 10.6$ GPa derived from the average shear wave velocity in the edifice. By using $\mu = 7$ GPa based on a previous interpretation of VLP data from Kilauea Volcano, Hawaii [Lane et al., 2001], we obtain a maximum volume change of $\Delta V = 200 \text{ m}^3$ for the Type-1 event.

[50] Accompanying the volumetric source components is a dominantly vertical force. Note that a single-force component must have an amplitude of approximately 10^{-3} N to excite signals whose amplitudes are comparable to the signals excited by a moment-tensor component of 1 Nm. Thus, the peak-to-trough amplitude of 2×10^8 N of the force observed in Figure 11 contributes roughly 5% of the signal amplitude relative to the contribution from the moment tensor.

[51] The source time functions derived for the Type-2 event (Figure 12) are relatively consistent with the picture elaborated above for the Type-1 event. The maximum volume

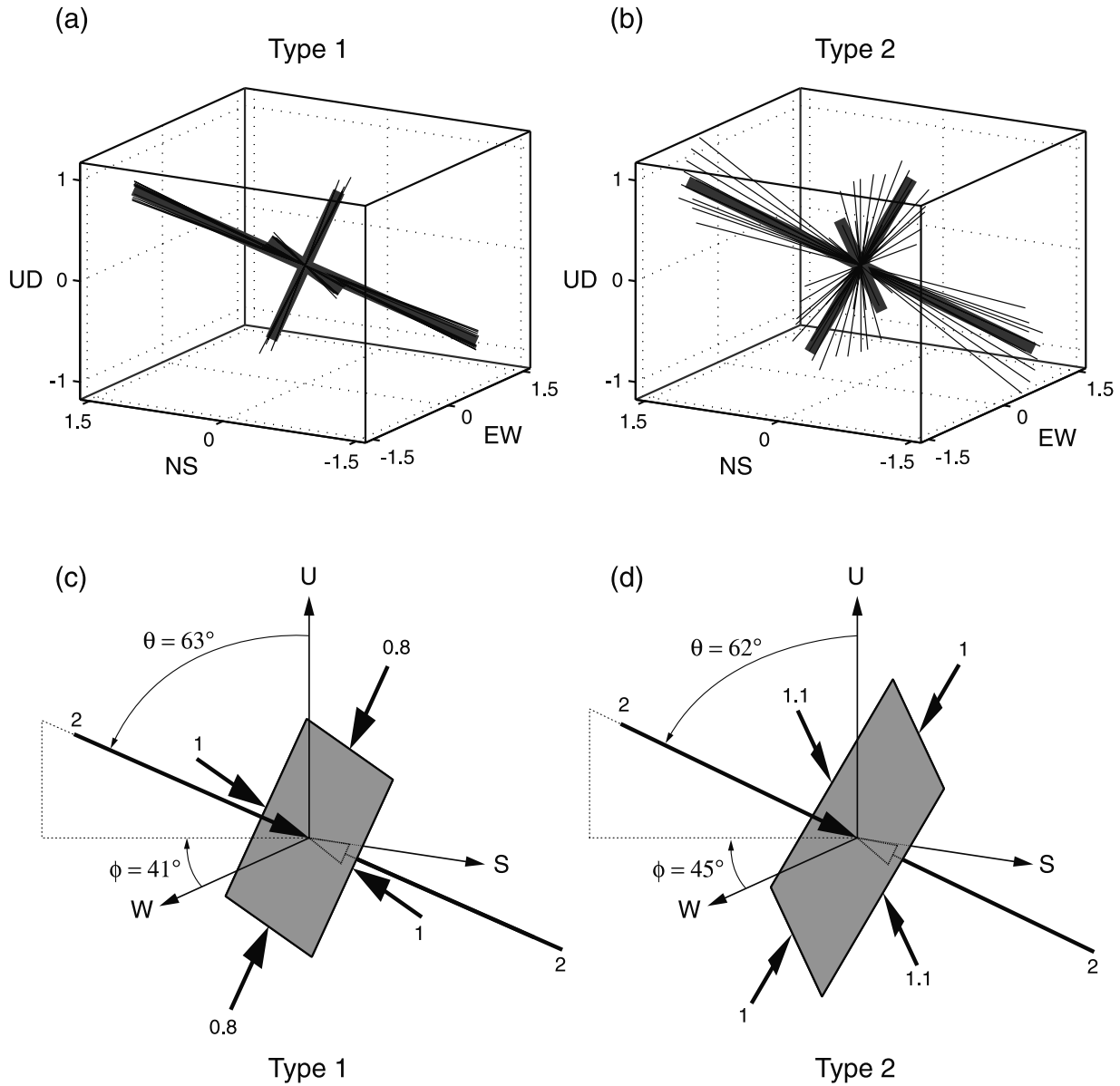


Figure 13. Source mechanisms obtained for Type-1 and Type-2 events. The reference coordinates for the eigenvectors are EW (east–west), NS (north–south), and UD (up–down). (a) Plot of eigenvectors for the moment-tensor solution shown in Figure 11; the eigenvectors are sampled every 0.3 s during the time interval 0–20 s. (b) Plot of eigenvectors for the moment-tensor solution shown in Figure 12; the eigenvectors are sampled every 1 s during the time interval 20–45 s. In both (a) and (b), the eigenvectors are normalized to a maximum length of 2 and no distinction is made between expansion and contraction. The thick grey lines show the eigenvectors obtained by measurements of maximum peak-to-trough amplitudes in Figures 11 and 12. (c) The three eigenvectors obtained from measurements of the maximum peak-to-trough amplitudes in the individual tensor components within the interval 0–20 s in Figure 11. (d) The three eigenvectors obtained from measurements of the maximum peak-to-trough amplitudes in the individual tensor components within the interval 20–45 s in Figure 12.

change is 170 m^3 . In that case the source time functions suggest a process that is **more extended in time** compared to Type-1 events. This conclusion is supported by visual observations of eruptive activity, which show longer durations ranging up to 20 s for these eruptions compared to durations of less than 10 s in Type-1 events, and suggest that the volumes of materials emitted during Type-2 events far exceed those released in Type-1 events.

Table 2. Source Mechanisms Calculated for Type-1 and Type-2 Events^a

Event	M_{xx}	M_{yy}	M_{zz}	M_{xy}	M_{yz}	M_{zx}	F_z	$\theta, ^\circ$	$\phi, ^\circ$
Type 1	41.0	38.0	29.3	-10.1	9.0	-10.5	2.0	63.2	40.8
Type 2	34.7	34.2	29.5	-8.1	7.2	-6.8	4.5	61.8	44.8

^aUnits are 10^{11} Nm for moment components and 10^8 N for force components. θ is the polar angle and ϕ is the azimuth (measured clockwise from the west direction) defining the orientation of the dominant dipole component of the source. The values listed for the M_{pq} components and F_z are peak-to-trough magnitudes.

[52] The sustained background of volumetric oscillations makes the identification of the eruption signal somewhat more difficult for the Type-2 event. The eruption is best identified by the vertical force, which shows a well-defined sequence of downward and upward forces. The sharp onset of the downgoing force, marked by the discontinuity in the slope of the signal near 24 s, coincides with an abrupt turn in the volumetric signal and rapid inflation of the dike. In contrast to Type-1 event, in which the initial dike inflation starts from the equilibrium state of the dike (zero volume change), **the inflation in Type-2 event starts from a partially collapsed state of the dike** (negative volume change) corresponding to a low pressure cycle at the source. Another significant aspect of the Type-2 source is the magnitude of the single force, which contributes roughly **13%** of the signal amplitude relative to the contribution from the moment tensor. We discuss the significance of these observations in more detail later in the paper.

7. Resolution Capabilities of the Method

[53] To test our inversion results we now address a few important questions concerning the resolution capabilities of the method. First, how precise is the method? We want to know if it reproduces the correct source mechanism and source time functions when these are known. Next, how sensitive is the method to errors in the source position or to an inadequate choice of medium velocities? And last, to what extent is there **a possible influence of dynamic tilt** in the VLP signals observed at Stromboli? These questions are explored below in the specific context of the source parameters and medium properties found at Stromboli. Unless specified otherwise, the medium velocities, medium topography and bathymetry, source location, and receiver positions used in calculating the synthetics are identical to those used in our earlier calculations of Green's functions. **Only receivers on the T and M grids are used in these tests.**

7.1. Reconstruction of Source Time Functions

[54] We first investigate the capability of our method to reconstruct a given source time function. We consider three source mechanisms: an isotropic source, an isotropic source combined with a single upward force, and a dipping crack combined with a single downward force. A cosine source time function $S(t) = [1 - \cos(2\pi t/t_p)]/2$ with $t_p = 3$ s is used for each source mechanism. The isotropic source is given by $M_{xx} = M_{yy} = M_{zz} = S(t) \times 1$ N m, and the single force attached to this source is given by $F_z = S(t) \times 10^{-3}$ N, with all other $M_{pq} = 0$ and $F_p = 0$. The crack has principal dipole components with amplitudes of $S(t) \times 1$, $S(t) \times 1$, and $S(t) \times 2$ N m, with a dominant dipole tilted 63° from the positive vertical axis and rotated 41° clockwise from west, and the associated single force is given by $F_z = -S(t) \times 1.45 \times 10^{-4}$ N, with the other $F_p = 0$. The physical processes corresponding to these source histories consist of: (1) an isotropic volume expansion followed by a recovery to the original volume; (2) an isotropic volume expansion followed by a recovery to the original volume, combined with a pulse-like upward force; and (3) a crack inflation followed by deflation back to the original crack volume, combined with a pulse-like downward force. This latter mechanism is representative of the model derived for Type-1 event (see Figures 11 and 13c).

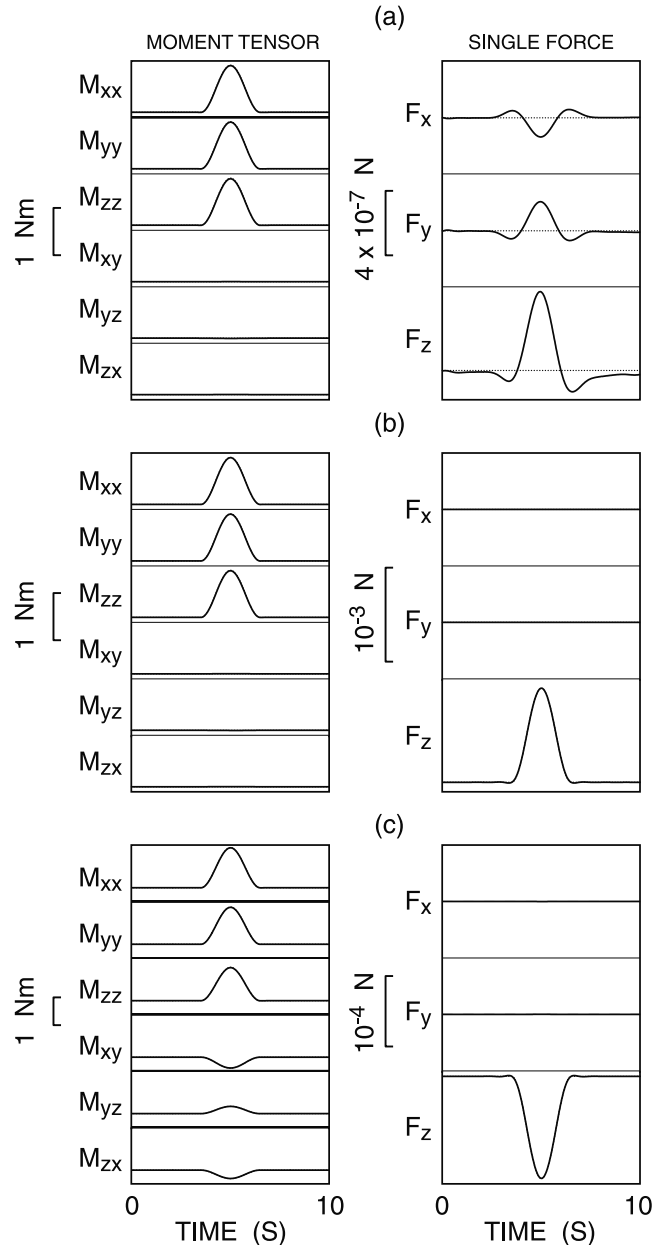


Figure 14. Numerical tests of the capability of our inversion method to reproduce known source time functions and combinations of source mechanisms. Dotted lines (visible only in (a)) show the given source time functions, and solid lines show the results of the inversion. The zero line for F_z has been shifted in each plot to optimize the amplitude scale used to represent the force components. (a) Reconstruction of an isotropic source. (b) Reconstruction of an isotropic source combined with a single upward force. (c) Reconstruction of a dipping crack combined with a single downward force. In both (b) and (c), the reconstructions are so good that the dotted-line curves are entirely beneath the solid curves, i.e., nearly all the differences are too small to be visible at the scale of the illustration.

[55] The inversion solutions to the given synthetic waveforms indicate that the source time functions of the purely volumetric source are well reconstructed (Figure 14a). Recall that a single-force component must have an ampli-

tude of roughly 10^{-3} N to excite signals with amplitudes comparable to those of signals excited by a moment-tensor component of 1 N m. Therefore, the single-force component with amplitude 0.5×10^{-6} N in Figure 14a is **negligible**, because it contributes less than 0.1% of the signal amplitude.

[56] The second test is specifically aimed at the capability of our method to decouple a dipole component from a force component with the same orientation. The Green's functions associated with M_{zz} and F_z are similar, so that these components may be difficult to decouple when the receiver coverage is limited [Uhira and Takeo, 1994]. In this test, the amplitudes of the force and dipole components are such that **their contributions to the radiated waveforms are of the same order of magnitude**. Our inversion results are depicted in Figure 14b, in which the given source time functions (dotted lines) plot precisely with the inversion results (solid lines). This shows that all the given elements of the source are properly recovered and confirms that both M_{zz} and F_z are well resolved with our network coverage.

[57] The third test demonstrates the capability of our method to reconstruct a source mechanism analogous to that derived by inversion of our VLP data. In this test, the single force contributes 10% of the seismic amplitudes. Our results (Figure 14c) show that all the significant components of the source mechanism are well reconstructed. 

7.2. Effects of Source Mislocations

[58] Although the location of the absolute minimum in the distribution of residual errors derived with equation (10) is well defined for both types of events (see Figure 8), the precision in our estimate of the source-centroid location is limited by the 40-m-size of the grid used in our search for the best fit source (see section 6.4). A conservative estimate of the location error is the grid interval. Therefore, the following tests assume a maximum source mislocation error of 40 m in the vertical, north–south and east–west directions.

[59] In these tests, the true source location is fixed to the position of the centroid for Type-1 event. The true source location refers to the source for which input synthetic seismograms are available, and the assumed source refers to the source for which the Green's functions used in the inversion are calculated. We investigate the effects of source mislocations on the inversion results for six mislocation errors as follows: (1) the assumed source is 40 m shallower than the true source depth; (2) the assumed source is 40 m deeper; (3) the assumed source is offset 40 m to the east; (4) the assumed source is offset 40 m to the west; (5) the assumed source is offset 40 m to the north; and (6) the assumed source is offset 40 m to the south. We assume a source mechanism analogous to that obtained for Type-1 event and consider a dipping crack with dominant dipole component tilted 63° from the positive vertical direction and rotated 41° clockwise from west (see Figure 13c). The principal dipole components have amplitudes of $S(t) \times 1$, $S(t) \times 1$, and $S(t) \times 2$ N m. Together with this mechanism is a single force given by $F_z = -S(t) \times 1.45 \times 10^{-4}$ N, which contributes 10% of the waveform amplitudes. All the source components are represented by a cosine source time function $S(t) = [1 - \cos(2\pi t/t_p)]/2$ with $t_p = 3$ s. Figures 15a–15f show the source–time functions obtained after inversion.

[60] The mislocation errors contribute 2–3% of the waveform amplitudes in the form of single-force components. The orientations, directions, and magnitudes of the single-force components induced depend on the source offset direction. Note in particular that the amplitude of the input downward force is reduced by 28% when the source is mislocated 40 m above (Figure 15a), and increased by 31% when the source is mislocated 40 m below the actual source (Figure 15b).

[61] For sources mislocated down (Figure 15b), east (Figure 15c), or south (Figure 15f), the ratios of the principal dipole components in the reconstructed source vary by less than 10% compared to the original ratios, while the orientation of the dominant dipole component differs by 2 to 7° from that of the original. The magnitude of the volume change is underestimated by 1 to 8%.

[62] Our results demonstrate that the distortion of the original source mechanism becomes pronounced when the source is mislocated closer to the free surface (Figures 15a, 15d, and 15e). Although the ratios of the principal dipole components are not strongly affected in a source mislocated 40 m west of the true source (Figure 15d), the orientation of the principal dipole component differs by 10° from that of the original. The worst results occur for a source mislocated 40 m north of the true source (Figure 15e). In that case, the orientation of the dominant dipole component differs by 15° from that of the original, and the ratios of the principal dipole components differ by up to 40% from the original ratios, mainly as the result of a strong underestimation of the M_{yz} component. The magnitude of the volume change is overestimated by 29% for a source mislocated above the true source (Figure 15a), and underestimated by 23% for a source mislocated to the west (Figure 15d), or 21% for a source mislocated to the north (Figure 15e).

7.3. Effects of Inadequate Velocity Models

[63] Error bounds in velocities are based on estimates obtained by Chouet *et al.* [1998]. Using these data, we assess the effect of our choice of velocities on the inversion results by calculating synthetic seismograms for two homogeneous media with respective compressional wave velocities $V_p = 3.0$ km/s and $V_p = 4.0$ km/s, shear wave velocity $V_s = V_p/\sqrt{3}$, and density $\rho = 2650$ kg/m³. We consider the same source mechanism as in Figure 15. In this test, the original Green's functions are calculated for the velocities $V_p = 3.5$ km/s, $V_s = 2$ km/s, and density $\rho = 2650$ kg/m³, so that the first model represents a case in which the velocities used in the reconstruction are higher than those of the true model for which the synthetic seismograms are calculated, and the second model represents the opposite situation.

[64] Our simulations show that the use of a faster velocity to calculate Green's functions leads to an overestimation of the original source mechanism by 59% and induces a downward single force F_z , which contributes 2% of the waveform amplitudes and magnifies the amplitude of the input downward force by 24% (Figure 16a). When we use a slower velocity, however, the result is an underestimation of the original source mechanism by 27% and a spurious upward single force F_z which contributes 2% of the waveform amplitudes and decreases the amplitude of the input

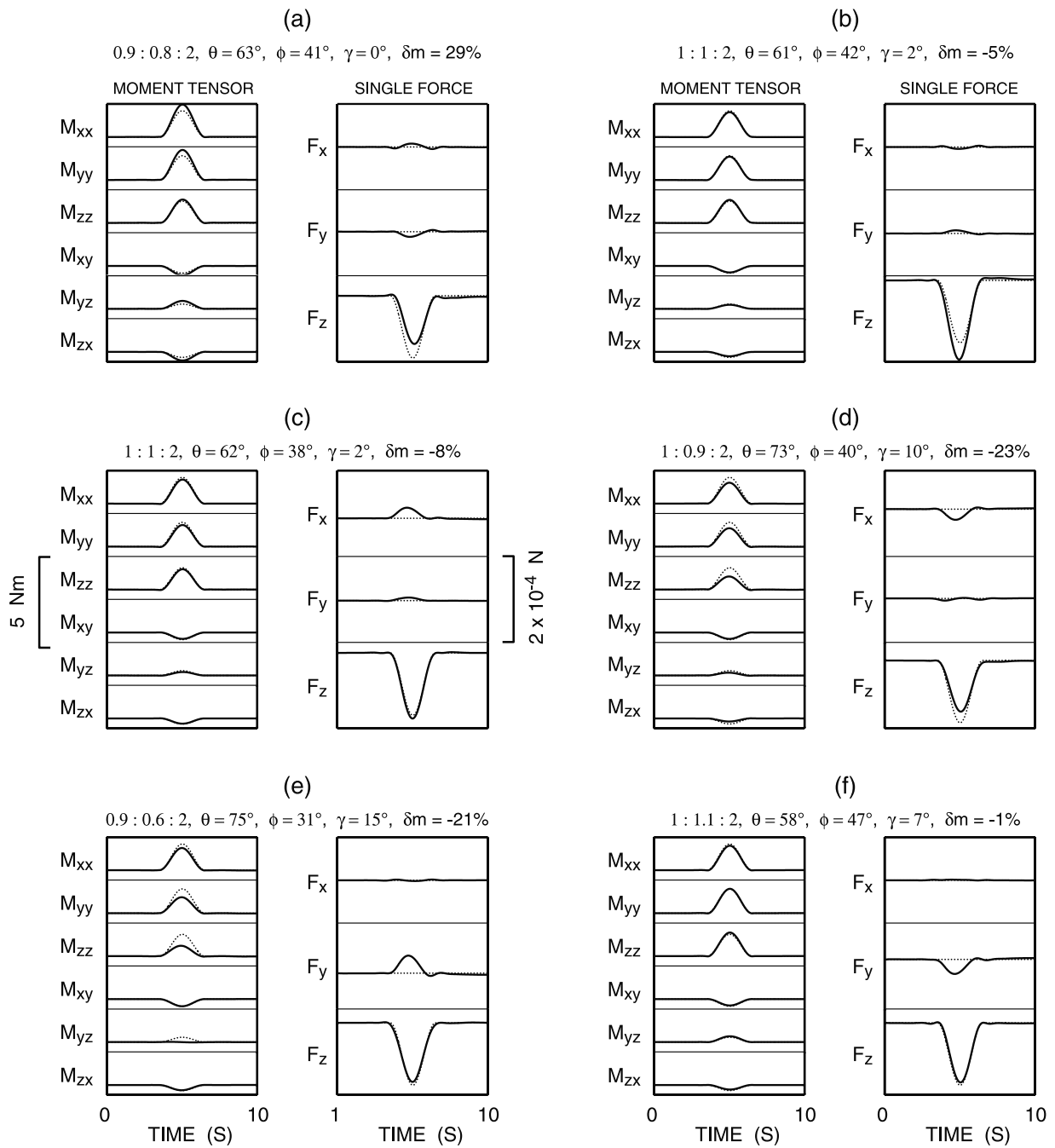


Figure 15. Effects of source mislocation on the reconstruction of a source mechanism consisting of a dipping crack combined with a single downward force. Dotted and solid lines have the same meaning as in Figure 14. The zero line for F_z has been shifted in each plot to optimize the amplitude scale used to represent the force components. (a) The reconstructed source is 40 m shallower than the true source. (b) The reconstructed source is 40 m deeper than the true source. (c) The reconstructed source is located 40 m east of the true source. (d) The reconstructed source is located 40 m west of the true source. (e) The reconstructed source is located 40 m north of the true source. (f) The reconstructed source is located 40 m south of the true source. The amplitude ratios of the principal dipole components and polar angle θ and azimuth ϕ (measured clockwise from the west direction) of the dominant dipole component, are indicated above each reconstruction, along with the angle γ between reconstructed and original dominant dipoles, and percentage error δm in the estimated magnitude of volume change.

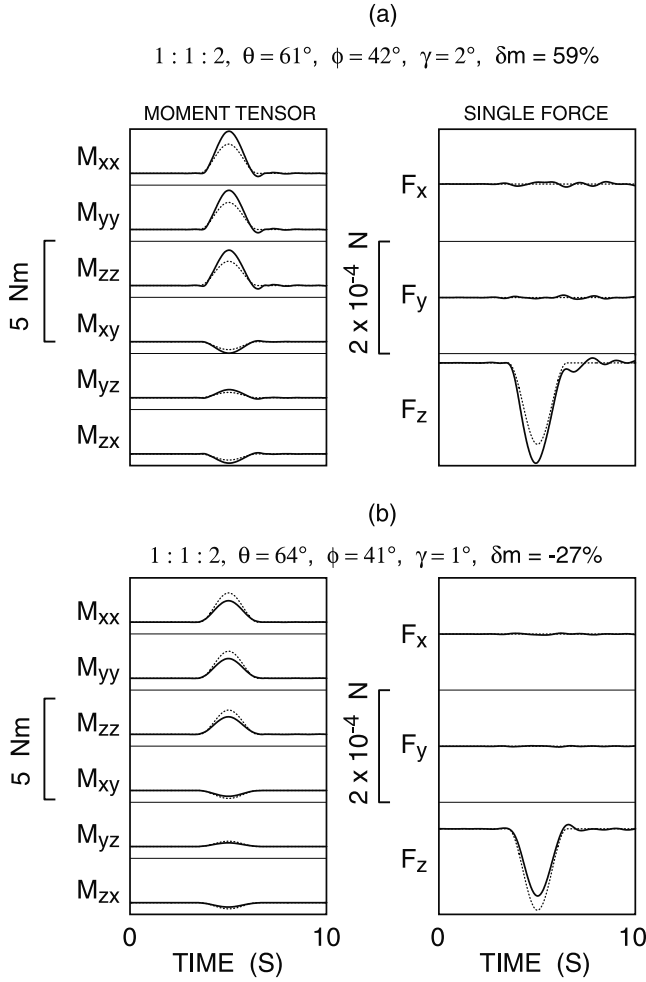


Figure 16. Effects of an inadequate velocity model on the reconstruction of a source mechanism consisting of a dipping crack combined with a single downward force. Dotted and solid lines have the same meaning as in Figure 14. (a) The velocities used in the reconstruction are higher than the true velocities. (b) The velocities used in the reconstruction are lower than the true velocities (see Figure 15 for details).

downward force by 18% (Figure 16b). There is, however, **little distortion in the derived source mechanism.**

7.4. Effect of Tilt

[65] Dynamic tilts induced by the sources may affect long-period horizontal seismometers through their sensitivity to gravitational acceleration, producing apparent horizontal displacements that are proportional to the second integral of the tilt-angle time history [Aki and Richards, 1980]. In contrast, for a precisely vertical sensor the effect of tilt is essentially negligible so that this sensor will show a pure displacement waveform. To first order, the apparent horizontal acceleration, $\ddot{u}_i(t)$, due to a time varying tilt or rotation, $\theta(t)$, is given by [Rodgers, 1968]

$$\ddot{u}_i(t) = -g\theta(t), \quad (13)$$

where g is the acceleration of gravity. Thus, a constant tilt gives rise to a step in acceleration. Equation (13) must be

integrated twice in the time domain to obtain the apparent displacement due to tilt. Tilt is computed by taking the curl of the displacement

$$\begin{aligned} \vec{\nabla} \times \vec{u} &= \vec{i} \left(\frac{\partial u_z}{\partial y} - \frac{\partial u_y}{\partial z} \right) + \vec{j} \left(\frac{\partial u_x}{\partial z} - \frac{\partial u_z}{\partial x} \right) + \vec{k} \left(\frac{\partial u_y}{\partial x} - \frac{\partial u_x}{\partial y} \right) \\ &= \vec{i}\theta_x + \vec{j}\theta_y + \vec{k}\theta_z, \end{aligned} \quad (14)$$

in which θ_x , θ_y , and θ_z are the rotations around the x , y , and z axes, respectively. The components of the curl are calculated at each receiver location by the finite difference method of Ohminato and Chouet [1997]. In this calculation, we use the source time functions calculated for Type-1 and Type-2 sources (Figures 11 and 12) as input source mechanisms. The horizontal components of displacements due to tilt are calculated using the x and y components of the curl of displacement. Note that θ_y acts on the x component of displacement and θ_x acts on the y component of displacement.

[66] The tilt signals associated with the source time functions in Figures 11 and 12 are shown in Figure 17. This figure compares the horizontal displacements due to pure translation to the horizontal displacements due to combined translational and rotational motions at station T6 where the synthetic tilt signal is strongest. The displacements due to the combined translational and rotational motions are shown both prior to and after band-pass filtering the signal in the 2–20 s band (Figure 17a) or the 2–30s band (Figure 17b), providing a comparative picture of the overall tilt contribution and residual tilt effect remaining in the signal after filtering. The results in Figure 17a show that the tilt contribution to horizontal displacements is trivial in Type-1 event; however, the effect of tilt is stronger in Type-2 event. **Most of the tilt contribution occurs at periods longer than 30 s**, so that band-pass filtering the signal in the 2–30 s band yields a signal in which the residual effect of tilt is only slightly more pronounced than in the synthetics of Type-1 event (Figure 17b). In both cases, **tilt does not markedly affect the shape of the band-passed waveforms at any station.** Based on these results, we conclude that our data are not biased by tilt effects.

8. Discussion

8.1. Reliability of the Solutions

[67] Our numerical tests indicate that **under noise-free conditions** various source mechanisms are well resolved by our network. Except for a source offset 40 m to the north, source mislocations have little effect on the solutions. The mislocation errors result mainly in an underestimation or overestimation of the magnitude of the volume change. Errors in the velocity model also mainly affect the absolute amplitudes of the tensor components in the solution but do not change the amplitude ratios among individual tensor components. The source location is also relatively unaffected by errors in velocities, because the location is fixed by waveform fits rather than travel times. Our uncertainty of ± 0.5 km/s in compressional wave velocity does not change the source mechanism but may

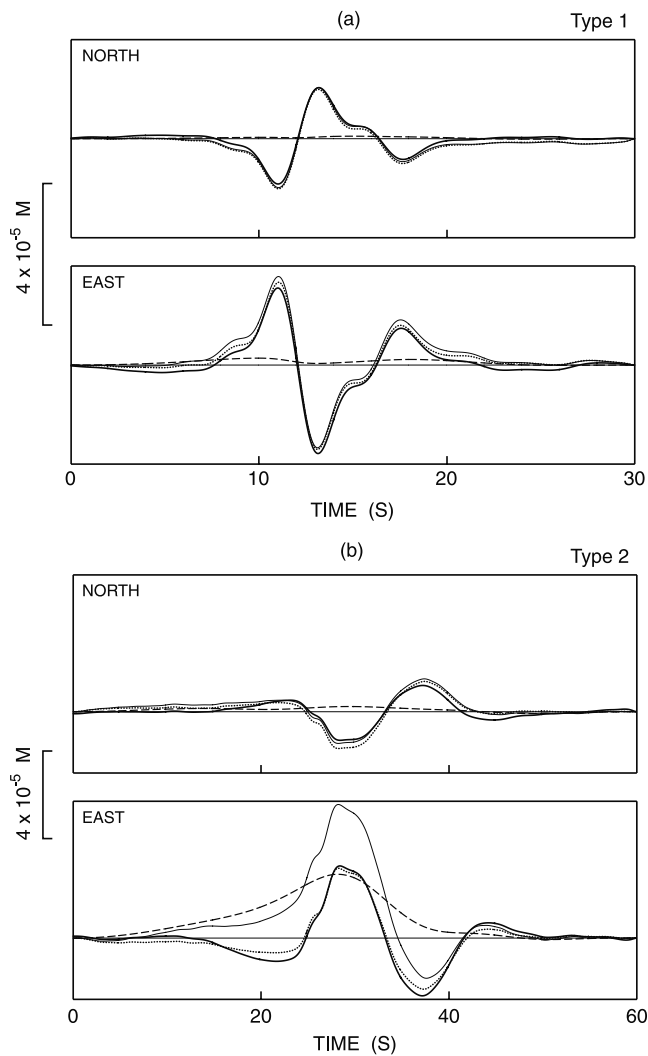


Figure 17. Effects of dynamic tilt on the displacement measured by the instrument at station T6. (a) Results for Type-1 event. (b) Results for Type-2 event. Dotted and dashed lines, respectively, show the displacement due to translation, and apparent displacement due to rotation obtained by integrating equation (13) twice in the time domain. Thin lines show the displacements due to the combined contributions of translation and rotation prior to filtering, and bold lines show the same displacements after filtering (see text for details).

cause an uncertainty of up to 60% in the estimated moment (Figure 16a).

8.2. Single Force

[68] Our numerical tests indicate that source mislocations or uncertainties in the velocity model may induce spurious force components in our solution (Figures 15–16). The spurious forces may contribute 2–3% of the signal amplitude relative to the contributions from the moment tensor. The contributions from the single-force components imaged in our solution are 5% in the Type-1 event, and 13% in the Type-2 event, roughly two to five times larger than possible contributions from spurious forces, and giving us confidence in the reality of the observed forces. Additional

observations lend further support to this conclusion. First, note that the spurious forces always point consistently in the direction of a source offset, unlike the bipolar forces imaged in our solutions. Note also that the behavior of the observed forces is consistent in the two events, and in both cases the contributions from downward and upward forces are roughly equivalent. If a significant spurious vertical force component were present in these solutions, one would expect that the symmetry between upward and downward forces would be completely broken, in contrast to what is observed. Finally, strong support for the validity of a single force in our solutions comes from the excellent quality of waveform fits in Figures 9 and 10, smaller residual errors, and minimal value of AIC calculated for a source mechanism involving both moment and force components versus the errors and AIC calculated for a source mechanism involving moment tensor components only (Table 1), and consistency among source time functions and robustness of overall source mechanisms derived when a single force is present. Therefore, we conclude that the waveforms of the vertical forces in our solution cannot be attributed to any spurious forces related to a 40-m vertical mislocation error in source location. Below we discuss the implication of this force for the process driving Strombolian eruptions.

[69] A single force can be generated by an exchange of linear momentum between the source and the rest of the Earth [Takei and Kumazawa, 1994]. Detailed examination of the time history of the single force sheds additional light on the origin of this force and its significance in the eruption dynamics. The force is initially directed down, then up. In the Type-1 event, the **downward force is synchronous with the initial inflation** of the source volume (see shaded interval in Figure 11), while the **following upward force is synchronous with the deflation** of the source volume. A downward force can be explained as the reaction force on the Earth associated with either an upward acceleration or downward deceleration of the center of mass of the source volume. Similarly, an upward force is consistent with either a downward acceleration or upward deceleration of the center of mass of the source volume. This suggests that, initially, **as the overpressured gas slug pushes the dike walls apart, it also acts piston-like to push the perched column of liquid above the slug upward**. The net result of this upward acceleration of heavier magma is an upward acceleration of the center of mass of the source volume. Visual observations of the vent area immediately prior to eruptions show that no magma is extruded from the conduit. Therefore, as the lighter slug of overpressured gas rises in the conduit toward the surface, it must deform to allow a downward flow of magma perched above the gas slug. **This counterflow of heavier magma results in a downward acceleration of the center of mass in the conduit, which is viewed here as the origin of the upward vertical force.**

[70] Momentum conservation requires that the net change of linear momentum in the overall source system must cancel out over the total duration of an event [Takei and Kumazawa, 1994], so that the downward single force must be counterbalanced by the upward single force. This is indeed observed to be the case in Figure 11.

[71] In addition to the vertical force components linked to shifting masses, there is also another force component acting on the source during the eruption. This extra force

component due to the jet recoil [Kanamori *et al.*, 1984, Figure A1] is downward-directed and may be active over some interval of time during the source deflation and reinflation phases. Unfortunately, it is not possible to separate the individual source time functions of vertical force components produced by mass movements from the pulse-like negative force associated with the jet recoil in our data, because our inversion only resolves the combined contributions of these forces.

[72] The single force imaged in the Type-2 event is consistent with the picture elaborated above for the Type-1 event, and again shows a net momentum exchange of zero over the total duration of the event. The perfect coincidence between volumetric inflation and downgoing force observed in Type-1 event is not so clear in the Type-2 event because of the contribution from background volumetric oscillations (compare shaded intervals in Figures 11 and 12).

[73] The estimated magnitudes of the downgoing forces are 0.8×10^8 N in Type-1, and 2.4×10^8 N in Type-2 event. To explore the implications of the three-fold difference in these forces within the physical framework outlined above, we neglect a possible contribution from jet recoil and assume that the observed forces solely reflects the forces required to lift the mass of liquid perched on top of the gas pocket.

[74] The maximum amplitude of the downgoing force in the Type-1 event coincides with the peak inflation of the dike (see shaded interval in Figure 11). The corresponding maximum volume expansion of the dike is 90 m^3 , that is roughly half of the maximum volume change (200 m^3) estimated earlier from the difference between maximum inflation and maximum deflation of the dike (see section 6.6). In spite of noticeable differences in the waveforms of the signals characterizing the volumetric and downgoing-force components in the Type-2 event (Figure 12), there is a similar coincidence between peak dike inflation and maximum amplitude of the downgoing force (see shaded interval in Figure 12). The corresponding maximum volume expansion of the dike is 100 m^3 , again roughly half of the maximum volume change estimated from the peak-to-trough amplitudes of the volumetric signals in Figure 12. In both Type-1 and Type-2 events, dike inflation is the result of a localized application of excess pressure over a small patch of wall on both sides of the overpressured gas pocket. To estimate the pressure in the gas pocket from the amplitude of the downgoing force we need to know the volume and shape of the gas pocket. For a rough estimation, we may assume a gas pocket in the form of a disk-shaped object slotted between the parallel walls of the dike, and assume also that the maximum volume expansion of the dike estimated from seismic data is a good estimate of the maximum volume of the gas pocket. Exposed dikes at Stromboli typically have thicknesses of a few meters [Tibaldi, 2001]. In an inclined dike, the body of the gas pocket may be concentrated on the upper wall and may or may not occupy the entire dike aperture depending on prevailing conditions at the source. We consider a gas pocket thickness of 1 m, which easily fits in a dike a few meters thick.

[75] In the Type-1 event, the maximum downward force of 0.8×10^8 N coincides with a maximum volume expansion of 90 m^3 at the source. Using a density for the

liquid of 2600 kg/m^3 and assuming the top 20 m of conduit are free of magma, the magmatic pressure is 5.1 MPa at the source centroid depth of 220 m. Approximating the gas pocket by a disk-shaped object with thickness of 1 m, radius of 5.35 m, and horizontal cross-section of 10.7 m^2 , one finds that the observed downward force implies a pressure in the gas pocket of 7.5 MPa, roughly 47% above the magmatic pressure.

[76] In the Type-2 event, the downward force of 2.4×10^8 N corresponds to a volume expansion of 100 m^3 at the source depth of 260 m. A gas pocket thickness of 1 m yields a horizontal cross-section of the gas pocket of 11.3 m^2 and gas pressure of 21.2 MPa, 3.5 times the magmatic pressure at this depth. A 2-m-thick gas pocket would yield a gas pressure of 15.0 MPa, 2.5 times the magmatic pressure. These estimates suggest gas pressures on the order of 10 MPa, consistent with independent estimates of initial pressure inferred by Vergnolle [1998] for a model of a pressurized bubble ascending in a vertical pipe filled with a viscous liquid.

[77] Assuming an ideal gas we may use the relation $pV/T = \text{constant}$ to estimate the volume erupted during an explosion. For simplicity we assume that the gas temperature remains constant so that this relation yields $p_a V_a = p_s V_s$, where p_a and p_s represent the atmospheric pressure and initial gas pressure, respectively, and V_a and V_s represent the volumes of gas at pressures p_a and p_s . In the Type-1 event, the ratio $p_s/p_a = 75$ and $V_s = 90 \text{ m}^3$ imply $V_a = 6.8 \times 10^3 \text{ m}^3$, and in the Type-2 event, the ratio $p_s/p_a = 212$ (for a gas pocket thickness of 1 m) and $V_s = 100 \text{ m}^3$ yield $V_a = 21.2 \times 10^3 \text{ m}^3$.

[78] The observed rate of eruptions and peak-to-peak signal amplitudes in Type-1 events (see Figure 2b) yields an overall volume eruption rate of $\sim 50 \times 10^3 \text{ m}^3/\text{hr}$. The eruption rate is $\sim 90 \times 10^3 \text{ m}^3/\text{hr}$ for Type-2 events. The combined volume eruption rate for Type-1 and Type-2 events is $\sim 140 \times 10^3 \text{ m}^3/\text{hr}$.

8.3. Factors Controlling the Intermittency of Eruptions

[79] The strikes of the two dikes imaged in our inversions are coincident with the main direction of diking identified in the edifice [e.g., Tibaldi, 2001]. The position and dip of the inclined dike imaged in the Type-1 event are such that the dike plane would intersect the surface at vent 1. The dike plane imaged in the Type 2 event similarly intersects the free surface at vent 2. This suggests that the shallow conduit system feeding these vents represents the mostly solidified upper parts of underlying en echelon fissures striking in the NE–SW direction. The dip angles of these dikes are also consistent with the inferred dips of sliding surfaces activated during the Sciara Del Fuoco collapse [Tibaldi, 2001].

[80] The seismic data presented here are at odds with the working assumption usually applied at Stromboli, in which the intermittency of eruptions is assumed to be a consequence of the periodic collapses of a foam layer formed by the accumulation of bubbles that remain trapped below the flat roof of a magma chamber [Jaupart and Vergnolle, 1988, 1989]. Jaupart and Vergnolle [1988, 1989] note that the essential phenomenon involved in the foam collapse is the deformation of bubbles by buoyancy forces as the bubbles tend to become more closely packed in the foam layer. The maximum packing condition is reached when the

contact area between bubbles becomes equal to the cross-sectional area of the bubble. There is a critical layer thickness above which bubble deformation becomes insufficient to balance buoyancy, at which point the foam layer collapses. While this model offers an elegant explanation for the Strombolian degassing regime, **our seismic data provide no compelling evidence supporting the presence of a shallow magma chamber at Stromboli**. A logical question therefore is: can similar slug flow regimes be induced in a slanted conduit without the need for a gas trap? To address this question a series of laboratory experiments were performed to investigate the release of single gas slugs in vertical and inclined tubes over a range of gas flow rates and liquid viscosities [Lane and Chouet, 2001].

[81] Flow patterns were observed for gas flow rates of 0.3–10 l/min in liquids with viscosities ranging from 10^{-3} to 10 Pa s in tubes with inclinations ranging between vertical and 45° from vertical [Lane and Chouet, 2001]. Bubbly flow (bubble diameter < tube diameter) was observed to occur in a vertical tube at low gas-flow rates. Increasing the gas-flow rate forced the pattern into a slug flow (bubble diameter = tube diameter). Inclining the tube had the result of forcing the transition from bubbly to slug flow at gas-flow rates roughly one order of magnitude lower than in vertical tubes.

[82] The results obtained by Lane and Chouet [2001] show that gas bubbles rising in an inclined liquid-filled tube tend to concentrate against the upper wall with the result that collisions between bubbles and coalescence of bubbles are greatly enhanced. Gas slugs are the inevitable outcome even at low gas-flow rates, and are the result of a local increase in gas-volume fraction due to bubbles concentrating against the upper wall, and slower speed of the bubbles traveling near the wall because of the effect of the wall on the flow pattern of the liquid around the bubble. The slower the bubbles travel, the higher the gas-volume fraction for a given gas input rate. The gas-volume fraction also goes up as viscosity increases for a given gas input rate. Slug flow becomes stable at a certain gas-volume fraction, and localized bubble concentration against inclined surfaces makes slug flow inevitable at all but the lowest gas-flow rates for nonvertical walled conduits. The actual conduit geometry may well be unimportant just as long as there is sufficient local bubble concentration at inclined surfaces to form slugs, the crucial difference here being the nonvertical versus vertical orientation of the conduit.

8.4. Factors Controlling Gas-Slug Formation

[83] The initial inflation of the source dike and uplift of liquid observed in seismic data may be linked to the release of surface tension and bubble expansion resulting from the breakdown of accumulated foam at the inclined wall of the source dike. The detailed dynamics of bubbles in a foam are poorly known, and the following discussion is based on the dynamics of a single spherical bubble embedded in an infinite incompressible liquid. Our simplifying assumption of an incompressible fluid is justified provided the radial velocity of the bubble wall remains much smaller than the sound speed of the bubbly liquid. At a depth of 200 m, the sound speed of a bubbly basalt with a gas-volume fraction of a few percent may range over a few hundred meters per second [Chouet, 1996], so that this assumption holds for

bubble expansion velocities up to a few tens of meters per second.

[84] Let us consider two bubbles, each of radius a , which are in contact with each other within the foam. The gas inside each bubble is at a pressure P_i above the ambient pressure P so that [Leighton, 1994]

$$P_i - P = \frac{2\sigma}{a}, \quad (15)$$

where σ is the surface tension. Upon bursting, the two bubbles coalesce into a single gas pocket. Under isothermal conditions the pressure inside the gas pocket is initially at the same pressure P_i , which is not in equilibrium with the surface tension provided by the larger surface boundary of the pocket. The result is an expansion of the gas inside the pocket, which promotes the bursting of bubbles surrounding the pocket. The pocket thus progressively enlarges by swallowing adjacent bubbles encountered in the foam. As the incipient pocket does not need to expand significantly to promote the bursting of neighboring bubbles, the driving pressure difference stays close to the value given by (15) [Jaupart and Vergnolle, 1989]. Once the supply of neighboring bubbles is exhausted, further growth of the pocket induced by the surface tension release is impeded by the viscosity and inertia of the surrounding bubbly liquid. The gas pressure in a growing bubble is given by the Rayleigh-Plesset equation [Plesset and Prosperetti, 1977; Leighton, 1994]

$$P_i = P + \frac{2\sigma}{a} + 4\eta\frac{\dot{a}}{a} + \rho_m \left[a\ddot{a} + \frac{3\dot{a}^2}{2} \right], \quad (16)$$

where \dot{a} is the radial velocity and \ddot{a} the radial acceleration of the bubble wall, η is the dynamic viscosity, and ρ_m is the bubbly liquid density. The three pressure terms in this equation are the static, surface tension pressure ($P_\sigma = 2\sigma/a$), and dynamic, viscous pressure ($P_\eta = 4\eta\dot{a}/a$) and inertial pressure ($P_\rho = \rho_m[a\ddot{a} + (3\dot{a}^2/2)]$).

[85] For initial bubble radii in the 10^{-3} – 10^{-2} m range [Jaupart and Vergnolle, 1988, 1989], with surface tension of 0.4 N/m [Walker and Mullins, 1981], the surface tension pressure is 80–800 Pa, far below the $P_i - P \sim 10^6$ Pa required for the expansion of the pocket at the source depth ~ 200 m. A simple dimensional analysis reveals the importance of the viscous and inertial terms relative to the surface tension term in (16). The magnitude of the viscous term is $\sim 4\eta/t_0$ and the magnitude of the inertia term is $\sim \rho_m a_0^2/t_0^2$, where a_0 is a scaling constant for bubble radius, and t_0 is the time scale of bubble expansion. The relevant value of a_0 here is the radius of the gas pocket, and t_0 is the time scale of pocket expansion. For a pocket volume ~ 100 m³ we may consider $a_0 \approx 3$ m. The time scale of pocket expansion must be shorter than the risetime in the source time histories in Figures 11 and 12, because these times depend on the propagation speed of the crack wave, which may be as slow as a few 10 m/s [see Chouet, 1996, Figure 14]. For a rough approximation we may assume $t_0 \approx 0.1$ – 1 s. We further assume $\rho_m = 2600$ kg/m³, and $\eta = 400$ Pa s [Vergnolle and Brandeis, 1996]. Then, the viscous term is on the order of 10^3 – 10^4 Pa, and the inertia term is on the order of 10^4 – 10^6 Pa.

[86] Our simple analysis suggests that the inertia term may contribute significantly to overpressure in a rapidly expanding large-size gas pocket. More accurate estimates of bubble overpressure would require a detailed analysis of the expansion dynamics of a large nonspherical gas pocket in a slab of compressible fluid bounded by two elastic walls. The interaction dynamics between the gas, liquid and solid are complex and an accurate description of these dynamics is left for future study.

9. Conclusions

[87] We used the method of *Ohminato et al.* [1998] to determine the source mechanisms of VLP signals associated with explosions at Stromboli Volcano, Italy. Our results provide an integrated view of the fundamental mechanisms underlying Strombolian explosions, as observed in September 1997. The observed VLP waveforms radiated by explosions are remarkably well fitted by simple point sources. Two source centroids were identified, representative of two distinct event types associated with eruptions from two different vents. The imaged source mechanisms include both moment-tensor and single-force components. The moment-tensor components are representative of two cracks dipping $\sim 60^\circ$ to the northwest and striking northeast-southwest along a direction coincident with the main direction of diking identified in the edifice. The two cracks are located 220 and 260 m beneath and ~ 160 m northwest of the active vents and may represent parts of an echelon system of fissures striking in the NE-SW direction. The dip angles of the two dikes are consistent with the inferred dips of sliding surfaces activated during the Sciara Del Fuoco collapse [Tibaldi, 2001]. The shallow depths of these dikes beneath the Sciara Del Fuoco, and orientations of the dikes in relation to the slope of the unconsolidated talus filling the Sciara, have important implications for the stability of the northwest flank of Stromboli.

[88] The maximum volume changes estimated from the moments are ~ 200 m³ for the largest explosion from each vent. Together with the volumetric source is a dominantly vertical force with magnitude of 10^8 N, consistent with the inferred movement of the magma column perched above the source centroid. The source time histories of the moment components display a characteristic sequence of inflation-deflation-inflation of the source volumes. The initial inflation represents a pressurization of the conduit attributed to the formation and release of a slug of gas. A stronger deflation follows, which reflects a lowering of the magmatic head associated with the rise and ejection of the slug. The next inflation marks a repressurization of the conduit caused by slumping of the liquid film surrounding the slug back to the top of the magma column after the slug has burst at the surface. The vertical force accompanying these volumetric motions is initially directed down, then up. The downward force is synchronous with the initial inflation of the source volume, while the following upward force is synchronous with the deflation of the source volume. This suggests that, initially, as the overpressured gas slug pushes the dike walls apart, it also acts piston-like to push upward the perched column of liquid above the slug. The net result of this upward acceleration of magma is an upward acceleration of the center of mass of the source

volume, which induces a downward reaction force on the Earth.  The lighter-than-magma slug of overpressured gas rises in the conduit toward the surface, it must deform to allow a downward flow of magma perched above the gas slug. This counterflow of heavier magma results in a downward acceleration of the center of mass in the conduit, which is viewed here as the origin of the upward vertical force.

[89] The seismic source mechanisms and observed intermittency of explosive eruptions are suggestive of a degassing process in which gas bubbles rising in the inclined liquid-filled dike tend to concentrate against the upper wall of the dike, thus enhancing the collisions between and coalescence of bubbles. As demonstrated in laboratory experiments with analog fluids, localized bubble concentration against inclined surfaces makes slug flow inevitable at all but the lowest gas-flow rates for nonvertical conduits. Therefore, a crucial element in this degassing process is the inclination of the conduit.

[90] The initial inflation of the source dike and uplift of liquid interpreted from the seismic data may be linked to the release of surface tension and subsequent gas-pocket expansion resulting from the breakdown of a foam raft at the inclined wall of the source dike. The downward force of 10^8 N and corresponding volume expansion at the source suggest gas pressures on the order of 10 MPa. For initial bubble radii in the 10^{-3} – 10^{-2} m range with surface tension of 0.4 N/m, the surface tension pressure is 80–800 Pa, far below the excess pressure required for the expansion of the gas pocket at the source depth. Crude analyses suggest that the inertia of the liquid surrounding the gas pocket may be a controlling factor leading to the large excess pressure inferred from seismic data.

[91] Based on the initial gas pressure and volume expansion at the source estimated from seismic data, and assuming a perfect gas at constant temperature, the volumes of gas ejected in the largest explosion from each vent are on the order of 10^4 m³. In comparison, photoballistic measurements of the size and number of particles carried by eruption jets [Chouet *et al.*, 1974] indicate that the volume of liquid ejected during an eruption is typically on the order of 10^{-1} m³, suggesting a characteristic volume ratio of liquid to gas of 10^{-5} . The observed rate of 20–30 explosive events per hour yields an overall gas-volume flow rate erupted on the order of 10^5 m³/hr for the two vents combined. This value for September 1997 may be typical of swarm activity at Stromboli at other times.

[92] **Acknowledgments.** We thank V. Augusti, P. Bernardini, R. Bianconi, M. Capello, G. Capone, M. Cattaneo, A. Cirella, M. Dal Bosco, V. D'Errico, C. Dietel, P. Chouet, L. Filippi, G. Gallo, S. Marcucci, M. Mattoni, M. Pasta, and E. Zambonelli for their participation in the field experiment. We are grateful to E. Privitera for his support in the field, and to C. Eva and P. Marsan for their support with instrumentation. The Italian Dipartimento della Protezione Civile and Guardia di Finanza provided invaluable helicopter support. We are indebted to David Hill, Robert Tilling, Michel Bouchon, an anonymous reviewer, and the Associate Editor of JGR for helpful suggestions. We also thank Javier Almendros for his help in converting the original manuscript from TEX to LATEX format. This research was supported through a grant from the Consiglio Nazionale delle Ricerche, Gruppo Nazionale di Vulcanologia.

References

Akaike, H., A new look at the statistical model identification, *IEEE Trans. Autom. Control*, AC-9, 716–723, 1974.

- Aki, K., and P. G. Richards, *Quantitative Seismology*, 932 pp., W. H. Freeman, New York, 1980.
- Braun, T., and M. Ripepe, Interaction of seismic and air waves recorded at Stromboli Volcano, *Geophys. Res. Lett.*, *20*, 65–68, 1993.
- Capaldi, G., et al., Stromboli and its 1975 eruption, *Bull. Volcanol.*, *41*, 1–27, 1978.
- Chouet, B., New methods and future trends in seismological volcano monitoring, in *Monitoring and Mitigation of Volcano Hazards*, edited by R. Scarpa and R. I. Tilling, pp. 23–97, Springer-Verlag, New York, 1996.
- Chouet, B., N. Hamisevicz, and T. R. McGetchin, Photoballistics of volcanic jet activity at Stromboli, Italy, *J. Geophys. Res.*, *79*, 4961–4976, 1974.
- Chouet, B., G. Saccorotti, M. Martini, P. Dawson, G. De Luca, G. Milana, and R. Scarpa, Source and path effects in the wavefields of tremor and explosions at Stromboli Volcano, Italy, *J. Geophys. Res.*, *102*, 15,129–15,150, 1997.
- Chouet, B., G. De Luca, G. Milana, P. Dawson, M. Martini, and R. Scarpa, Shallow velocity structure of Stromboli Volcano, Italy, derived from small-aperture array measurements of Strombolian tremor, *Bull. Seismol. Soc. Am.*, *88*, 653–666, 1998.
- Chouet, B., G. Saccorotti, P. Dawson, M. Martini, R. Scarpa, G. De Luca, G. Milana, and M. Cattaneo, Broadband measurements of the sources of explosions at Stromboli Volcano, Italy, *Geophys. Res. Lett.*, *26*, 1937–1940, 1999.
- Del Pezzo, E., C. Godano, A. Gorini, and M. Martini, Wave polarization and location of the source of the explosion quakes at Stromboli Volcano, in *Volcanic Seismology*, edited by P. Gasparini, R. Scarpa, and K. Aki, pp. 279–296, Springer-Verlag, New York, 1992.
- Gabbianelli, G., C. Romagnoli, P. L. Rossi, and N. Calanchi, Marine geology of the Panarea–Stromboli area (Aeolian Archipelago, Southern Tyrrhenian Sea), *Acta Vulcanol.*, *3*, 11–20, 1993.
- Hornig-Kjarsgaard, I., J. Keller, U. Koberski, E. Stadlbauer, L. Francalanci, and R. Lenhart, Geology, stratigraphy and volcanological evolution of the island of Stromboli, Aeolian arc, Italy, *Acta Vulcanol.*, *3*, 21–68, 1993.
- Jaupart, C., and S. Vergnolle, Laboratory models of Hawaiian and Strombolian eruptions, *Nature*, *331*, 58–60, 1988.
- Jaupart, C., and S. Vergnolle, The generation and collapse of a foam layer at the roof of a basaltic magma chamber, *J. Fluid Mech.*, *203*, 347–380, 1989.
- Julian, B. R., A. D. Miller, and G. R. Foulger, Non-double-couple earthquake mechanisms at the Hengill-Grensadalur volcanic complex, southwest Iceland, *Geophys. Res. Lett.*, *24*, 743–746, 1997.
- Kanamori, H., and J. W. Given, Analysis of long-period waves excited by the May 18, 1980, eruption of Mount St. Helens—A terrestrial monopole?, *J. Geophys. Res.*, *87*, 5422–5432, 1982.
- Kanamori, H., and J. Mori, Harmonic excitation of mantle Rayleigh waves by the 1991 eruption of Mount Pinatubo, Philippines, *Geophys. Res. Lett.*, *19*, 721–724, 1992.
- Kanamori, H., J. W. Given, and T. Lay, Analysis of seismic body waves excited by the Mount St. Helens eruption of May 18, 1980, *J. Geophys. Res.*, *89*, 1856–1866, 1984.
- Kaneshima, S., et al., Mechanism of phreatic eruptions at Aso Volcano inferred from near-field broadband seismic observations, *Science*, *273*, 642–645, 1996.
- Kawakatsu, H., Centroid single force inversion of seismic waves generated by landslides, *J. Geophys. Res.*, *94*, 12,363–12,374, 1989.
- Kawakatsu, H., S. Kaneshima, H. Matsubayashi, T. Ohminato, Y. Sudo, T. Tsutsui, K. Uhira, H. Yamasato, H. Ito, and D. Legrand, Aso94: Aso seismic observation with broadband instruments, *J. Volcanol. Geotherm. Res.*, *101*, 129–154, 2000.
- Kikuchi, M., and H. Kanamori, Inversion of complex body waves, *Bull. Seismol. Soc. Am.*, *72*, 491–506, 1982.
- Kikuchi, M., and H. Kanamori, Inversion of complex body waves, *2, Phys. Earth Planet. Inter.*, *43*, 205–222, 1986.
- Kikuchi, M., and H. Kanamori, Inversion of complex body waves, *3, Bull. Seismol. Soc. Am.*, *81*, 2335–2350, 1991.
- Kirchdörfer, M., Analysis and quasistatic FE modeling of long period impulsive events associated with explosions at Stromboli Volcano (Italy), *Ann. Geophys.*, *42*, 379–390, 1999.
- Kumagai, H., T. Ohminato, M. Nakano, M. Ooi, A. Kubo, H. Inoue, and J. Oikawa, Very-long-period seismic signals and caldera formation at Miyake Island, Japan, *Science*, *293*, 687–690, 2001.
- Lane, S. J., and B. A. Chouet, The effect of conduit inclination on eruptive style, *Eos Trans. AGU*, *82(47)*, Fall Meet. Suppl., Abstract F1272, 2001.
- Lane, S. J., B. A. Chouet, J. C. Phillips, P. Dawson, G. R. Ryan, and E. Hurst, Experimental observations of pressure oscillations and flow regimes in an analogue volcanic system, *J. Geophys. Res.*, *106*, 6461–6476, 2001.
- Legrand, D., S. Kaneshima, and H. Kawakatsu, Moment tensor analysis of near-field broadband waveforms observed at Aso Volcano, Japan, *J. Volcanol. Geotherm. Res.*, *101*, 155–169, 2000.
- Leighton, T. G., *The Acoustic Bubble*, 613 pp., Academic Press, New York, 1994.
- Murase, T., and A. R. McBirney, Properties of some common igneous rocks and their melts at high temperatures, *Geol. Soc. Am. Bull.*, *84*, 3563–3592, 1973.
- Neuberg, J., R. Luckett, M. Ripepe, and T. Braun, Highlights from a seismic broadband array on Stromboli Volcano, *Geophys. Res. Lett.*, *21*, 749–752, 1994.
- Nishimura, T., H. Nakamichi, S. Tanaka, M. Sato, T. Kobayashi, S. Ueki, H. Hamaguchi, M. Ohtake, and H. Sato, Source process of very long period seismic events associated with the 1998 activity of Iwate Volcano, northeastern Japan, *J. Geophys. Res.*, *105*, 19,135–19,147, 2000.
- Ohminato, T., and B. A. Chouet, A free-surface boundary condition for including 3D topography in the finite difference method, *Bull. Seismol. Soc. Am.*, *87*, 494–515, 1997.
- Ohminato, T., B. A. Chouet, P. B. Dawson, and S. Kedar, Waveform inversion of very-long-period impulsive signals associated with magmatic injection beneath Kilauea volcano, Hawaii, *J. Geophys. Res.*, *103*, 23,839–23,862, 1998.
- Pasquaré, G., L. Francalanci, V. H. Garduño, and A. Tibaldi, Structural and geological evolution of the Stromboli Volcano, Aeolian Islands, Italy, *Acta Vulcanol.*, *3*, 79–89, 1993.
- Plesset, M. S., and A. Prosperetti, Bubble dynamics and cavitation, *Annu. Rev. Fluid Mech.*, *9*, 145–185, 1977.
- Ripepe, M., and T. Braun, Air-wave phases in Strombolian explosion-quake seismograms: A possible indicator for the magma level?, *Acta Vulcanol.*, *5*, 201–206, 1994.
- Ripepe, M., and E. Gordeev, Gas bubble dynamics model for shallow volcanic tremor at Stromboli, *J. Geophys. Res.*, *104*, 10,639–10,654, 1999.
- Ripepe, M., M. Rossi, and G. Saccorotti, Image processing of the explosive activity at Stromboli, *J. Volcanol. Geotherm. Res.*, *54*, 335–351, 1993.
- Ripepe, M., P. Poggi, T. Braun, and E. Gordeev, Infrasonic waves and volcanic tremor at Stromboli, *Geophys. Res. Lett.*, *23*, 181–184, 1996.
- Ripepe, M., S. Ciliberto, and M. Della Schiava, Time constraints for modeling source dynamics of volcanic explosions at Stromboli, *J. Geophys. Res.*, *106*, 8713–8727, 2001.
- Rodgers, P. W., The response of the horizontal pendulum seismometer to Rayleigh and Love waves, tilt, and free oscillations of the earth, *Bull. Seismol. Soc. Am.*, *58*, 1385–1406, 1968.
- Romagnoli, C., P. Kokelaar, P. L. Rossi, and A. Sodi, The submarine extension of the Sciarra Del Fuoco feature (Stromboli Island): Morphologic characterization, *Acta Vulcanol.*, *3*, 91–98, 1993.
- Saccorotti, G., and E. Del Pezzo, A probabilistic approach to the inversion of data from a seismic array and its application to volcanic signals, *Geophys. J. Int.*, *143*, 249–261, 2000.
- Saccorotti, G., B. A. Chouet, M. Martini, and R. Scarpa, Bayesian statistics applied to the location of the source of explosions at Stromboli Volcano, Italy, *Bull. Seismol. Soc. Am.*, *88*, 1099–1111, 1998.
- Takei, Y., and M. Kumazawa, Why have the single force and torque been excluded from seismic source models?, *Geophys. J. Int.*, *118*, 20–30, 1994.
- Tibaldi, A., Multiple sector collapses at Stromboli Volcano, Italy: How they work, *Bull. Volcanol.*, *63*, 112–125, 2001.
- Uhira, K., and M. Takeo, The source of explosive eruptions at Sakurajima Volcano, Japan, *J. Geophys. Res.*, *99*, 17,775–17,789, 1994.
- Uhira, K., H. Yamasato, and M. Takeo, Source mechanism of seismic waves excited by pyroclastic flows observed at Unzen Volcano, Japan, *J. Geophys. Res.*, *99*, 17,757–17,773, 1994.
- Ukawa, M., and M. Ohtake, A monochromatic earthquake suggesting deep-seated magmatic activity beneath Izu-Oshima Volcano, Japan, *J. Geophys. Res.*, *92*, 12,649–12,663, 1987.
- Vergnolle, S., Modeling two-phase flow in a volcano, *Proceedings of 13th Australasian Fluid Mechanics Conference, Melbourne*, pp. 647–650, Aristoc Offset, Monash Univ., Melbourne, Australia, 1998.
- Vergnolle, S., and G. Brandeis, Strombolian explosions, 1, A large bubble breaking at the surface of a lava column as a source of sound, *J. Geophys. Res.*, *101*, 20,433–20,447, 1996.
- Voight, B., H. Glicken, R. J. Janda, and P. M. Douglass, Catastrophic rockslide-avalanche of May 18, in *The 1980 eruptions of Mount St.*

- Helens*, edited by P. W. Lipman and D. R. Mullineaux, *U.S. Geol. Surv. Prof. Pap. 1250*, U. S. government printing office, Washington, D. C., pp. 347–378, 1981.
- Walker, D., and O. Mullins Jr., Surface tension of natural silicates from 1200–1500°C and implications for melt structure, *Contrib. Mineral. Petrol.*, *76*, 455–462, 1981.
- Wassermann, J., Locating the sources of volcanic explosions and volcanic tremor at Stromboli Volcano (Italy) using beam-forming on diffraction hyperboloids, *Phys. Earth Planet. Inter.*, *104*, 271–281, 1997.
- Widmer, R., and W. Zürn, Bichromatic excitation of long-period Rayleigh and air waves by the Mount Pinatubo and El Chichón volcanic eruptions, *Geophys. Res. Lett.*, *19*, 765–768, 1992.
- Wielandt, E., and T. Forbriger, Near-field seismic displacement and tilt associated with the explosive activity of Stromboli, *Ann. Geofis.*, *42*, 407–416, 1999.
-
- B. Chouet and P. Dawson, U.S. Geological Survey, 345 Middlefield Road, MS 910, Menlo Park, CA 94025, USA. (chouet@usgs.gov; dawson@usgs.gov)
- G. De Luca and G. Milana, Servizio Sismico Nazionale, Rome, Italy.
- F. Giudicepietro, M. Martini, and G. Saccorotti, Osservatorio Vesuviano, Naples, Italy.
- T. Ohminato, University of Tokyo, Tokyo, Japan.
- R. Scarpa, Università di Salerno, Salerno, Italy.